ELECTRONICALLY STEERABLE ANTENNA ARRAY USING

PCB-BASED MEMS PHASE SHIFTERS

Except where reference is made to the work of others, the work described in this thesis is my own or was done in collaboration with my advisory committee. This thesis does not include proprietary or classified information.

____

Ananth Sundaram

Certificate of Approval:

____

Lloyd S. Riggs
Professor
Electrical and Computer Engineering

____

Ramesh Ramadoss, Chair
Assistant Professor
Electrical and Computer Engineering

____

Stuart M. Wentworth
Associate Professor
Electrical and Computer Engineering

____

Stephen L. McFarland
Dean
Graduate School

Electronically Steerable Antenna Array using PCB-based MEMS Phase Shifters

Ananth Sundaram

A Thesis

Submitted to

the Graduate Faculty of

Auburn University

in Partial Fulfillment of the

Requirements for the

Degree of

Master of Science

Auburn, Alabama
August 7, 2006

ELECTRONICALLY STEERABLE ANTENNA ARRAY USING

PCB-BASED MEMS PHASE SHIFTERS

Ananth Sundaram

Permission is granted to the Auburn University to make copies of this thesis at its discretion, upon the request of individuals or institutions and at their expense. The author reserves all publication rights.

____

Signature of Author

____

Date of Graduation

THESIS ABSTRACT

ELECTRONICALLY STEERABLE ANTENNA ARRAY USING

PCB-BASED MEMS PHASE SHIFTERS

Ananth Sundaram

Master of Science, August 7, 2006
(M. S. E. E, University of South Florida, Tampa, USA 2003)

91 Typed Pages

Directed by Ramesh Ramadoss

In this thesis, a novel approach for cost effective fabrication and assembly of MEMS based Electronically steerable antenna (ESA) arrays' using flexible printed circuit processing techniques has been developed. The critical component of the MEMS ESA is a 3-bit phase shifter that is implemented using MEMS varactors, where each phase shifter consists of two MEMS varactors. The important feature of this approach is the use of flexible circuit film, kapton E polyimide film, as the movable membrane in the MEMS varactors used in the phase shifters that are used for the beam steering of the antenna. The important features of this approach are:

a) The characteristic size is in the millimeter range and therefore the required dimensional tolerance and alignment accuracy can be achieved using conventional printed circuit processing techniques.

b) Batch fabrication of such antennas can be accomplished using existing roll-to-roll flexible printed circuit technology.

c) Beam steering angles of more than 10° can be easily attained.

The ESA consists of three layers – polyimide film, spacer, and substrate. The Polyimide film, which is capable of withstanding millions of mechanical flexing cycles, is used as the movable phase shifter membrane layer. Phase shifter top electrode is defined on the polyimide film that forms the movable membrane. Coplanar waveguide (CPW) defined on the metallization layer of the substrate is used as the phase shifter bottom electrode. The spacer layer provides the required spacing between the substrate layer and the polyimide film layer. A dielectric layer spin-coated on CPW metallization is used to provide a capacitive contact in the phase shifter down position. Pull-down voltages for the MEMS varactors used in the phase shifters are in the range of 100 - 200 Volts.

Design, modeling, and characterization of analog phase shifters, digital phase shifters and a folded slot antenna array are discussed. Beam steering performances of more than 10° for a two element MEMS ESA have been presented.

Dedication

This thesis is dedicated to my Guru Maharaj, Shree Swami Samarth.

ACKNOWLEDGEMENTS

I would like to sincerely thank my thesis advisor, Dr. Ramesh Ramadoss for his constant help and guidance in showing me the way at every juncture during the two and a half years of my attempts at successful completion of research here at Auburn University. I would especially like to thank him for his patience throughout my time of study here as I know even I would not have been as patient with myself as long as he was with me.

A special mention for supporting me throughout my many bittersweet educational endeavors goes to my parents and my grandmother.

I would also like to thank my very good friends, Neeraj Kulkarni, Nikhil Raj Mathur, and Anjani Kumar for constantly helping me discriminate between right and wrong in every facet of life. Many thanks to my companions here at Auburn, Vikas, Muthubalaji, Jithendra, Kapil, Madhu, Ramraj, Lia, Ron, Brian, Ramraj, and the rest for putting up with me for two and a half years.

Last but not the least; I am grateful to Sathya, Mugdha and Balaji for their continued support even after a few of my very important decisions and actions were not in agreement with their views.

Special thanks to Charles, William, Linda, Joe, Drew, Roger and Shakeeb for the good times in and out the Fab Lab.

Thanks everybody.

Style manual of journal used Graduate School: Guide to preparation and submission of theses and dissertations

Computer software used Microsoft Office XP

TABLE OF CONTENTS

LIST OF FIGURES…..……………………………………………………...……...xi

LIST OF TABLES..…..…………………………………………………………….xv

1 INTRODUCTION AND OVERVIEW 1

2 ESA DESIGN 5

2.1 Introduction.. 5
2.2 MEMS Based ESAs.. 5
2.3 ESA Configuration 5
2.4 ESA Component Design.. 8
2.4.1 Power Divider Design.. 8
2.4.2 Antenna Design.. 9
2.4.2.1 X-Band Slot Antenna design 9
2.4.2.2 Folded Slot Antenna Design:... 11
2.4.2.3 Quarter wave impedance transformer design: 12
2.4.2.4 Two Folded Slot Antenna Spaced 3λ/4 apart: 14
2.4.2.5 Beam-steering Characteristics 15

3 PHASE SHIFTER DESIGN 19

3.1 Analog type RF-MEMS Phase Shifters. 19
3.2 Bi-stable Varactor based phase Shifter design 23
3.2.1 Equivalent Circuit Model.. 24

4 FABRICATION AND EXPERIMENTAL CHARACTERIZATION 31

4.1 Fabrication and Assembly 31
4.1.1 Substrate – CPW line:... 31
4.2 Bonding film... 33
4.3 Kapton Film:... 33
4.3.1 Machining the Kapton film:... 34
4.4 Experimental Characterization 36
4.4.1 Fabrication Run #1:.. 36
4.4.2 Fabrication Run #2:.. 39
4.4.3 Fabrication Run #3.. 42

5 SUMMARY AND FUTURE WORK 45

5.1 Summary 45
5.2 Design 45
5.3 Fabrication and Assembly 46
5.4 Experimental Characterization 46
5.5 Future Work 46

BIBLIOGRAPHY 47

APPENDICES 51
A FABRICATION AND PROCESSING DETAILS 52
A.1 Fabrication and Processing Details 52
A.2 Layout Creation 53
A.3 Glass Mask Preparation 53
A.4 Substrate Layer 53
A.4.1 Machining and Drilling 53
A.4.2 Defining Pattern 53
A.4.2.1 Photolithography 54
A.4.3 Etching 56
A.4.4 BCB coating Process 57
A.4.4.1 UV Exposure 58
A.4.4.2 Development Procedure 58
A.4.4.3 Hard Bake 58
A.4.4.4 Curing 58
A.5 Switch membrane Layer 59
A.5.1 Top Electrode Patterning 59
A.5.2 DRIE Etching 60
A.6 Adhesive spacer film machining 60

B A KOCH FRACTAL ANTENNA 61
B.1 Introduction 61
B.2 Theory, design and Results 61
B.3 Simple Slot Antenna 62
B.4 Folded Slot Antenna 64
B.5 Folded Slot Antenna with Koch Iteration (type 1) 66
B.6 Folded Slot Antenna with Koch Iteration (type 2) 68
B.7 Folded Slot Antenna with Koch Iteration (type 3) 70
B.8 Tunable fractal folded Slot Antenna 73
B.9 Discussion and Conclusion 75

LIST OF FIGURES

2.1 (a)Top view of ESA (b) Cross sectional view of ESA. (not to scale). 7

2.2 CPW power divider layout showing optimized design parameters. 9

2.3. Return loss and Insertion loss for the Power Divider. 9

2.4. Initial slot antenna design. 10

2.5. Performance of the initial slot antenna design. (a) Return Loss, and (b) Real and Imaginary parts of the Input Impedance. 10

2.6. Folded Slot antenna layout.. 11

2.7. Performance of the Folded slot antenna design (a) Return Loss, and (b) Real and Imaginary parts of the Input Impedance. 12

2.8 Folded-slot antenna with quarter-wave matching tranformer (Antenna Design parameters remain unchanged). 13

2.9. Performance of the matched folded slot antenna (a) Return loss, and (b) Real and Imaginary parts of the Input impedance. 14

2.10. Two folded slot antennas placed 3λ/4 apart.. 14

2.11.Performance of the two folded slot antenna spaced 3λ/4 apart. (a) and (b) present return loss and input Impedance data, respectively, for the slot antenna element on the left side in Figure 2.10, (c) and (d) present return loss and input Impedance data, respectively, for the slot antenna element on the right side in Figure 2.10. 17

2.12. Simulated beam steering characteristics of the antenna array in the H-plane for various phase shifts (Port A fed with zero phase shifted signal and port Port B fed with the phase shifted signal (Ø) (Figure 2.10)). 18

3.1 Schematic of a mainline type loaded line phase shifter. 20

3.2 Layout of the loaded line type phase shifter with two MEMS varactors................... 21

3.3. Phase shifter insertion loss for various gap heights. 22

3.4. Phase shift corresponding to various gap heights of the MEMS varactors. 22

3.5. Cross section of bi-stable MEMS varactor in (a) up-state, (b) down-state................ 23

3.6. (a) Schematic of the MEMS varactor in up-state, (b) equivalent circuit model showing various capacitances and (c) equivalent circuit model with single equivalent capacitance. 24

3.7. MEMS varactor top view (not to scale). 26

3.8. Insertion losses for various Bi-stable phase shifter units in the 3-bit phase shifter with 14 um thick SU-8 as the dielectric layer. 27

3.9. Phase delay for various Bi-stable phase shifter units in the 3-bit phase shifter with 14 um SU-8 as the dielectric layer. 27

3.10. Insertion losses for various Bi-stable phase shifter units in the 3-bit phase shifter with 12 um thick BCB as the dielectric layer. 29

3.11. Phase delay for various Bi-stable phase shifter units in the 3-bit phase shifter with 12 um BCB used as the dielectric layer. 29

4.1 Antenna Pattern with BCB coating on RT/Duroid 6002. 32

4.2. Milled Bonding film. 32

4.3. Bottom side of Kapton film after the use of dummy masks (not to scale). 33

4.4. Kapton film with MEMS electrodes defined using actual mask (not to scale). 33

4.5. Aluminum mask layer on the Kapton for DRIE process (not to scale). 34

4.6. Kapton mask layer for DRIE Etching. 35

4.7. Cross section of Kapton showing patterned aluminum DRIE mask (not to scale). ... 35

4.8. Cross section of Kapton layer after DRIE (not to scale). 35

4.9. Kapton layer after the DRIE process. 36

4.10. Fabricated Two-element X-band electronically steerable Antenna Prototype. 37

4.11. Measured return losses of the ESA prototype corresponding to two beam states. .. 38

4.12. Antenna H-plane radiation patterns for the zero phase shifted signal (beam 1) and phase shifted signal (beam 2) fed to the right antenna element in the two-element array.38

4.13. Photograph of the ESA fabricated in Run #2 with BCB dielectric layer and air bridges. 40

4.14. Measured return loss for the ESA prototype from Run #2 with a) State 1 when all MEMS varactors in up position corresponding to zero phase shift condition, and b) State 2 when all MEMS varactors on the left side are in the down position. 41

4.15. Antenna H-plane measured radiation patterns for the zero phase shifted signal (beam 1) and phase shifted signal (beam 2) fed to the right antenna element in the two-element array. 41

4.16 Measured return loss for the ESA prototype from Run #3 with up-state and states with different MEMS phase shifters actuated from the left side of the Antenna array. ... 43

4.17. Measured return loss for the ESA prototype from Run #3 with up-state and states with different MEMS phase shifters actuated from the right side of the Antenna array. . 43

4.18. ESA #3 H-Plane radiation pattern with different phase shifters actuated. Phase shifter Units #1, #2 and #3 have been illustrated in Figure 4.10 44

A.1 Fabrication Steps and flow.. 52

A.2. BCB Curing Procedures.. 59

B.1 A Simple Slot Antenna... 62

B.2 Return Loss and Real and Imaginary parts of input impedance for the simple slot antenna. 63

B.3 Radiation Pattern for the simple slot Antenna (E Plane) 63

B.4 Layout of a folded slot antenna 64

B.5 Return Loss and Real and Imaginary parts of input impedance for a matched folded slot antenna. 65

B.6 Radiation Pattern for the folded slot Antenna (E plane). 65

B.7 Layout of a folded slot antenna with Koch Iteration (type 1). 66

B.8 Return Loss and Real and Imaginary parts of input impedance for a matched folded slot antenna with Koch Iteration (type 1). 67

B.9 Radiation Pattern for the folded slot Antenna with Koch iteration (type 1) (E plane) 67

B.10 Layout of a folded slot antenna with Koch Iteration (type 2). 68

B.11 Return Loss and Real and Imaginary parts of input impedance for a matched folded slot antenna with Koch Iteration (type 2) 69

B.12 Radiation Pattern for the folded slot Antenna with Koch iteration (type 2) (E plane) 69

B.13. Layout of a folded slot antenna with Koch Iteration (type 3). 70

B.14. Photograph of the fabricated Fractal Antenna with diode mounted for tuning purposes. 72

B.15. Measured and Simulated return loss results for the type 3 Koch fractal antenna. .. 73

B.16. Return losses of the tunable fractal antenna for various applied bias voltages....... 74

B.17. Measured and Simulated antenna radiation patterns for the first iteration Koch fractal antenna at 8.05 GHz (a) E-plane co-polarization (E_θ) pattern, (b) E-plane cross-polarization (E_ϕ) pattern, (c) H-plane co-polarization (H_θ) pattern, and (d) H-plane cross-polarization (H_ϕ). 75

B.18. Measured antenna radiation patterns for the tunable CPW Koch fractal Antenna at different frequencies corresponding to the bias voltages. (a) E plane co-polarization, (b) E

plane cross-polarization, (c) H plane co-polarization and (d) H plane cross-polarization. 76

LIST OF TABLES

2.1 Beam steering angle of the antenna array for various phase shifts (port P1 fed with zero phase shift signal and port P2 fed with phase shifted (Ø) signal)............................ 16

3.1. Design parameters for the phase shifters with 14 um thick SU-8 used as the dielectric layer.. 26

3.2. Design parameters for the phase shifters with 12 um thick BCB used as the dielectric layer.. 28

B.1 Resonant frequency, Return Loss and Input Impedance of an unmatched slot antenna 63

B.2 Resonant frequency, Return Loss and Input Impedance of an matched folded slot antenna 65

B.3 Layout and performance of a matched type 1 Koch fractal slot antenna.................. 67

B.4 Layout and performance of a matched type 2 Koch fractal slot antenna.................. 70

Chapter 1 INTRODUCTION AND OVERVIEW

Electronically scanned/steerable antennas (ESA) or phased array antennas use electronic, micro-electromechanical, or material switches to alter the phase of individual radiating elements across an antenna aperture, and in so doing, enable the radiated beam to steer without any mechanical motion of the antenna system. ESAs have broad applicability for both commercial and military applications and are currently being utilized in advanced military radars, cellular base stations, some satellite communications applications and other communication systems. Multiple beams can be radiated by a single ESA to enable detecting, tracking, and communicating with multiple objects simultaneously. ESAs have been used for ground, ship, and airborne radars, and in several satellite systems. However, their complexity and cost has limited their wider use in space [1]-[3]. Future uses for ESAs include automotive anti-collision radar, smart navigation systems, and improved wireless communications.

Traditional phased array antennas have been constructed with active electronics integrated with every radiating element. These electronic circuits typically include a phase shifter for setting the beam position and amplification to overcome the losses of the phase shifter and establish output power or noise figure of the system. The cost of such electronic circuits is typically quite high, of the order of $1000-$2000 for each antenna

element, making such electronically scanned antennas very expensive to build [4]. Due to the expensive nature of this type of antenna architecture, it has not been aggressively deployed in military radar and communication systems.

The cost of these antennas can be lowered by using “passive” array approaches where each radiator is driven by an ultra-low loss phase shifter, and where multiple radiator/phase shifters are fed by a single electronics module. For antenna arrays that have relatively low radiated power (<0.5 watts/radiator), this is very cost effective as it amortizes the expensive electronics over 4, 8, or 16 radiators [4]. However, this architecture requires phase shifter losses to be considerably lower than are realized with conventional microwave electronics technology. As an example, typical pin-diode or GaAs FET based 4-bit phase shifters incur 4-5 dB of loss at X-band while at Ka-band the losses are in the range of 8-10 dB which are high to be used in this type of architecture [4]. These high insertion losses reduce the phased array antenna's Effective Isotropic Radiated Power. The advent of MEMS technology has enabled phase shifters with considerably lower loss, allowing the realization of passive, electronically scanned antenna arrays.

In the past decade, RF Micro Electro Mechanical System (RF MEMS) switches and phase shifters that exhibit excellent characteristics including lower insertion loss and lower DC power consumption compared to their GaAs etc. based electronic counterparts have been demonstrated ([5]-[20]). Conventional RF MEMS phase shifters fabricated using surface micromachining techniques are not appropriate for integration with antennas on Printed Circuit Board (PCB) substrates, due to process incompatibility,

complexity and cost issues. Therefore, there is a need for low cost, printed-circuit compatible, RF MEMS technology for realization of low cost MEMS-based electronically scanned antenna array systems. Recently, RF-MEMS phase shifters fabricated using printed circuit processing techniques have been reported by our group [21]. These phase shifters are suitable for monolithic integration with low cost ESAs on Teflon or Polyimide like low dielectric constant PCB substrates. In this thesis, an electronically steerable antenna array integrated with RF MEMS phase shifters fabricated using PCB processing techniques is discussed.

Chapter 2 of this thesis starts with an overview of the configuration and principle of operation of the proposed ESA and then proceeds to explain the design of the components of the ESA namely, the power divider and the Antenna elements. The performances of the designed components are validated by Electromagnetic simulations.

Chapter 3 explains the design of two types of phase shifters, namely, the Analog type and the Digital type, and justifies the selection of the digital type of phase shifters for use in this work. All designs presented are accompanied with simulation results obtained from Electromagnetic Simulation software [22] .

Chapter 4 explains the fabrication of the complete ESA structure carried out by thermo-compression bonding of three layers explained in the configuration section in Chapter 2. Also, the experimental characterization of the ESA and phase shifters is discussed.

The thesis is then concluded in Chapter 5 by summarizing the design, fabrication and experimental characterizations of the ESA. Ideas for improving the results obtained in this work are also discussed in this chapter.

Chapter 2 ESA DESIGN

2.1 Introduction

In the previous chapter, the need for the development of MEMS based Electronically steerable antennas was discussed. This chapter provides the reader with the details of the configuration of the ESA, design process of the various components of the ESA and results from the respective simulations are discussed. This chapter is organized as follows: First, the configuration and principle of operation of the proposed ESA are discussed and then the design of the ESA components, the power divider and the Antenna elements are discussed.

2.2 MEMS Based ESAs

The complete configuration of the proposed PCB MEMS based ESA is shown in Figure 2.1. The ESA comprises of three components namely, the antenna element, the phase shifters and the power divider. In the following sections, the configuration of the ESA and design of the power divider and the antenna elements are described.

2.3 ESA Configuration

The ESA consists of three main layers: a Kapton E Polyimide film membrane (2 mils) with 3 μm thick copper metallization, an RT/Duroid 6002 Teflon substrate (30 mils) with 9 μm thick copper metallization, and a Polyflon adhesive spacer film (2 mils). The antenna structure and Coplanar Waveguide (CPW) lines are patterned using lithography techniques on the substrate copper metallization. The copper metallization on

the bottom side of the Kapton membrane is patterned to define the MEMS varactor top electrode. The polyflon spacer film provides the initial gap height for the MEMS varactor. MEMS varactors are biased using 250 Å thick and 50 μm wide resistive Nichrome bias lines with a resistivity of 1.1×10^{-6} Ω-m. A 14 μm thick SU-8 dielectric layer (Fabrication Run #1, Chapter 4) is spin-coated on the CPW line metallization to provide a capacitive contact in the down state for the MEMS varactors. These three layers, namely Kapton film, Polyflon film, and Duroid, are laminated by thermo-compression bonding to obtain the ESA prototype. Details of the fabrication and assembly procedures for similar structures are described in Chapter 4 of this thesis.

The phase shifter has been implemented using MEMS varactors fabricated using printed circuit based MEMS technology [28]. In this configuration, a 3-bit phase shifter has been designed by cascading three one-bit phase shifter units. A one-bit phase shifter unit consists of two identical MEMS varactors separated by a center-to-center distance of quarter wavelength as indicated in Figure 2.1(a). The configuration in Figure 2.1(b) depicts the initial position of the MEMS varactors. For operation, a DC bias voltage is applied to pull down the MEMS varactor membrane such that the top electrode is in contact with the dielectric layer (down state). The capacitance increase in the down state provides the required phase shift in the phase shifter, which enables desired steering of the antenna beam.

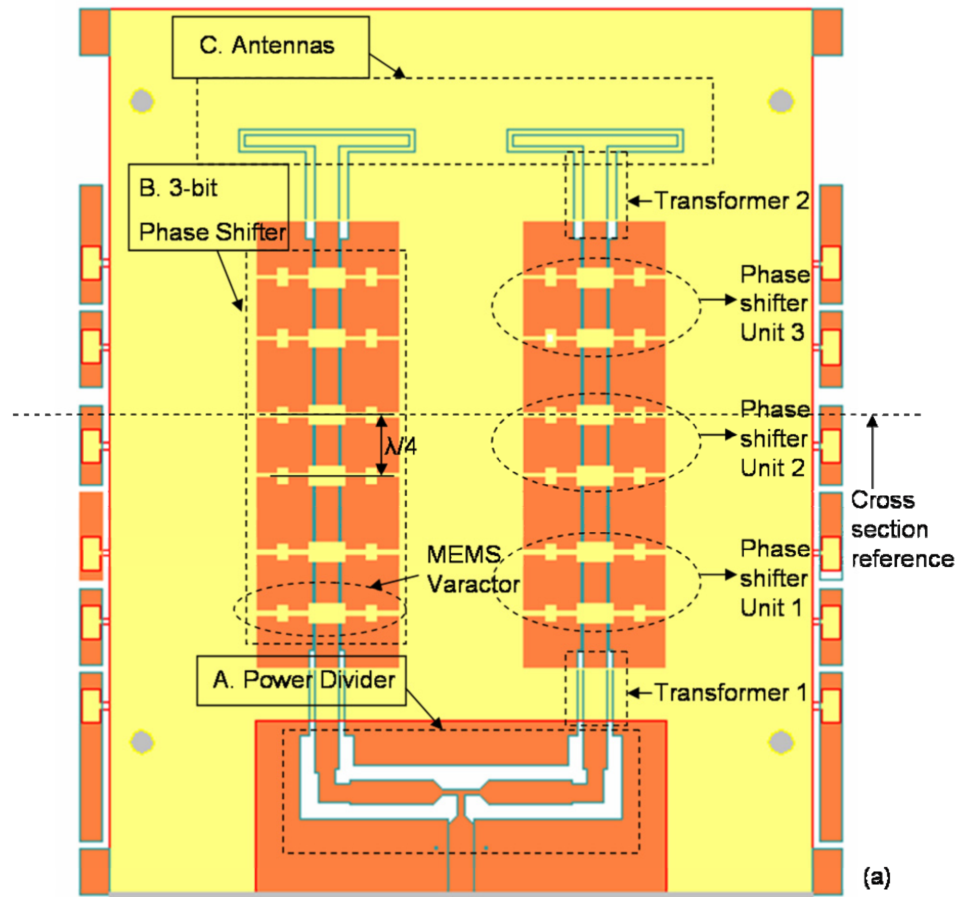

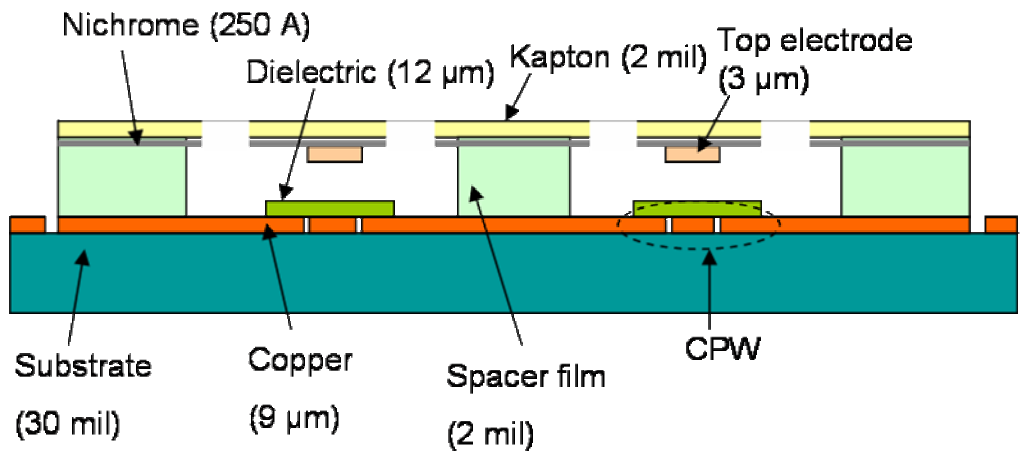

Figure 2.1 (a)Top view of ESA (b) Cross sectional view of ESA. (not to scale).

2.4 ESA Component Design

In this section, design and simulation of two ESA components, namely the power divider and antenna elements are described.

2.4.1 Power Divider Design

A CPW power divider has been designed for feeding the two element antenna array. The power divider consists of a 50 Ohm input line and two 100 Ohm output lines. Each output line is matched to the 3-bit phase shifter using a quarter-wave transformer (Transformer 1 in Figure 2.1(a)). To minimize the junction discontinuity effects, the configuration shown in Figure 2.2 with narrow inductive sections at the junction of the power divider has been implemented. This configuration of the power divider minimizes the capacitive discontinuity effect at the T-junction (where the input 50 Ohm line branches into two 100 Ohm lines). Also, compensated right angled bends were used to connect the power divider and the phase shifters [23]. Air bridges are used to suppress the excitation of slot modes at the T-junction and right-angle bends in the power divider [23]. Electromagnetic simulation and design optimization of the power divider design have been carried out in ADS Momentum [22]. S-parameter results of the optimized power divider design (design parameters shown in Figure 2.2) are shown in Figure 2.3. The input return loss at port 1 and the insertion loss between the input port (port 1) and output ports (ports 2 and 3) are about 10 dB and 3.8 dB, respectively, at 10 GHz.

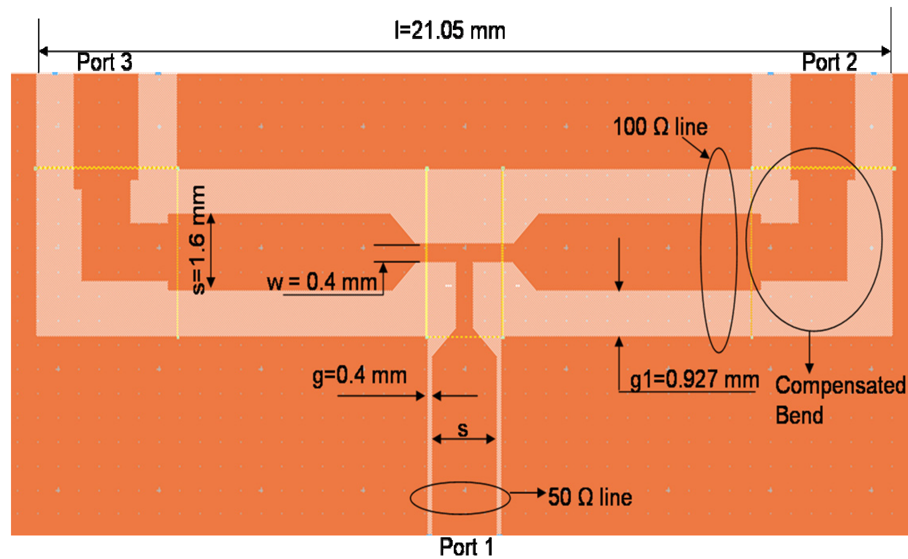

Figure 2.2 CPW power divider layout showing optimized design parameters.

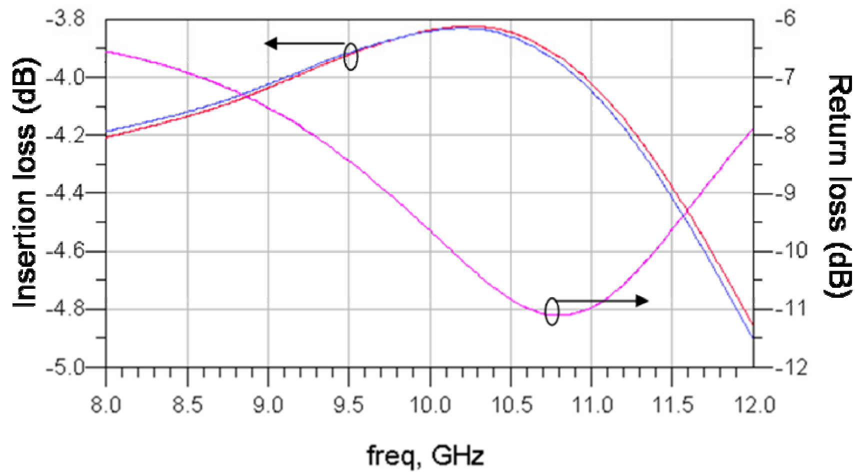

Figure 2.3. Return loss and Insertion loss for the Power Divider.

2.4.2 Antenna Design

2.4.2.1 X-Band Slot Antenna design

Initially, a $\lambda/2$ center fed slot antenna fed by a CPW feed line (shown in Figure 2.4) was designed for operation at 10 GHz. The width of the slot antenna was chosen to

be W = 0.4 mm. The guide wavelength λ_s of a 0.4 mm wide slot line on a 30-mil thick Duroid 6002 (ε_r = 2.94) was obtained to be 24 mm at 10 GHz from EM simulation in ADS Momentum (a 2.5D EM simulator available in ADS [22]). Then, the length of the slot antenna ($\lambda_s/2$ @ 10 GHz) was calculated to be L=12 mm. The antenna is fed by a 50 Ω (G/S/G = 0.1/1.6/0.1 mm) CPW feed line. This design has been simulated in HP-Momentum and the results are shown in Figure 2.5.

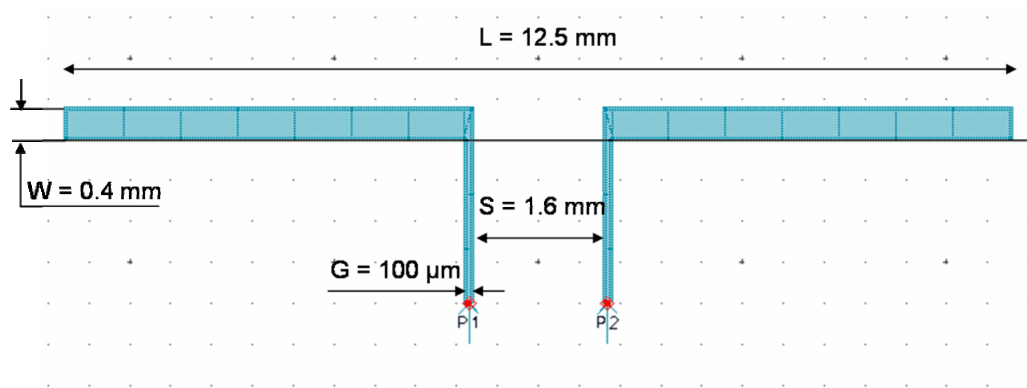

Figure 2.4. Initial slot antenna design.

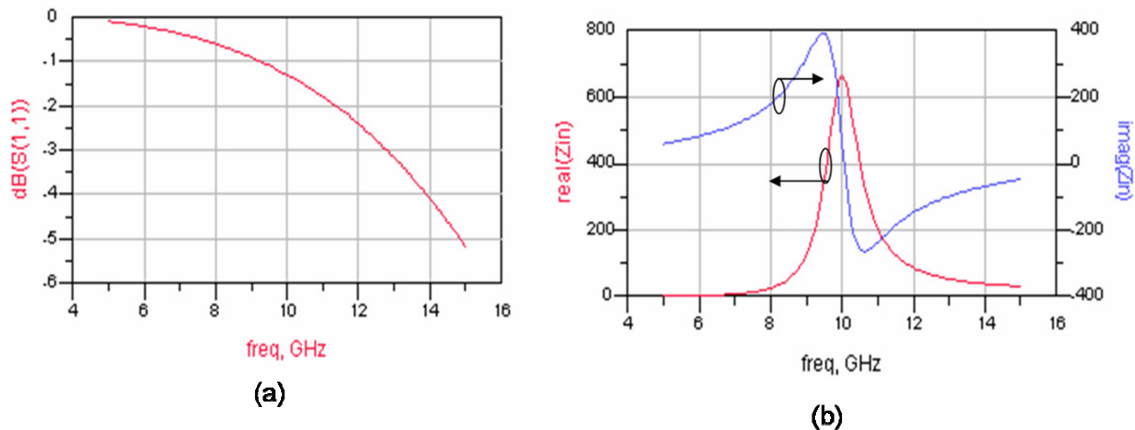

Figure 2.5. Performance of the initial slot antenna design. (a) Return Loss, and (b) Real and Imaginary parts of the Input Impedance.

From Figure 2.5(b), it can be noted that the antenna resonates (Imaginary(Zin) ~ 0) at 10 GHz but the antenna is not matched because the real part of the input impedance is about 650 Ω. To obtain a good match to the 100 Ω line, the real part of the input impedance must be decreased significantly (say less than 200 Ω). In order to decrease the input impedance of the slot antenna, a folded slot antenna design was considered and the details are discussed in the next section.

2.4.2.2 Folded Slot Antenna Design:

The input impedance of a slot antenna can be scaled down by adding slots in parallel and is governed by the equation (1) [23],

$$Z_{in} = \frac{Z_{slot}}{N^2} \quad (1)$$

where N is the number of slots in the antenna. Using this concept, the input impedance of the single slot antenna discussed earlier can be decreased to about 160 Ω (650 Ω/2^2) by adding one more slot in parallel as shown in Figure 2.6.

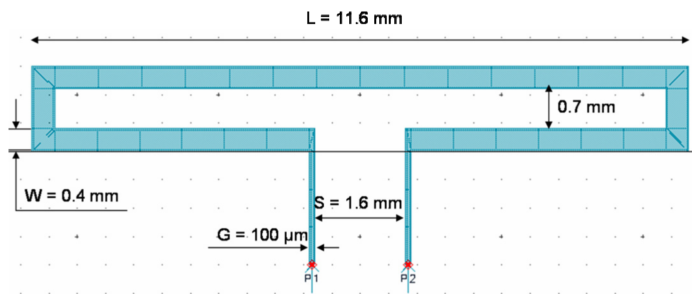

Figure 2.6. Folded Slot antenna layout.

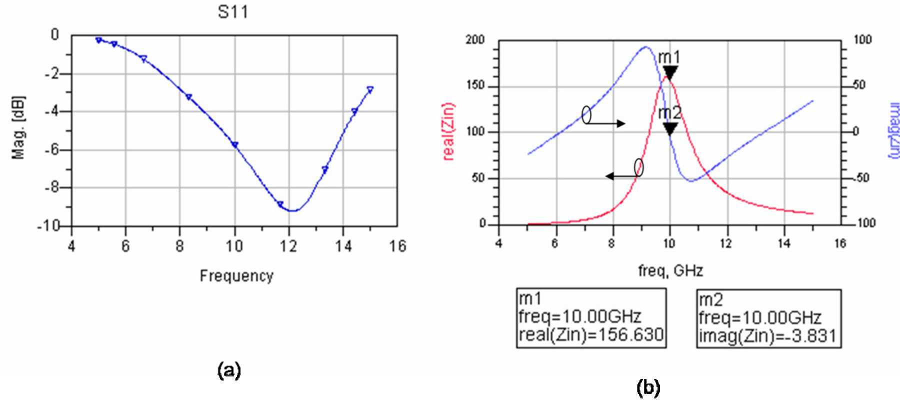

Figure 2.7. Performance of the Folded slot antenna design (a) Return Loss, and (b) Real and Imaginary parts of the Input Impedance.

From EM simulations, the length of the slot antenna has been optimized to a final value of L = 11.6 mm for operation at 10 GHz. From Figure 2.7(b), it can be seen that the antenna resonates (Imaginary(Zin) ~ 0) at the desired frequency of 10 GHz and the real part of the input impedance has been reduced to 156 Ω. The return loss has been improved by using a quarter wave impedance transformer between the antenna and the 50 Ω feed line, the design details of which are discussed in the next section.

2.4.2.3 Quarter wave impedance transformer design:

To transform an impedance of 156 Ω to 50 Ω, the impedance of the quarter wave transformer should be equal to [23]

$$Z_Q = \sqrt{Z_{in} Z_0} = \sqrt{156 \times 50} = 88.3\Omega$$

A CPW line that provides a characteristic impedance value of 88.3 Ω has been designed using [22] and the dimensions are: G/S/G = 0.6/1.6/0.6 mm on Duroid 6002. Length of the quarter wave CPW matching section is about 5.7 mm ($\lambda_g/4$ at 10 GHz). The layout of the folded slot antenna with the matching section is shown in Figure 2.8.

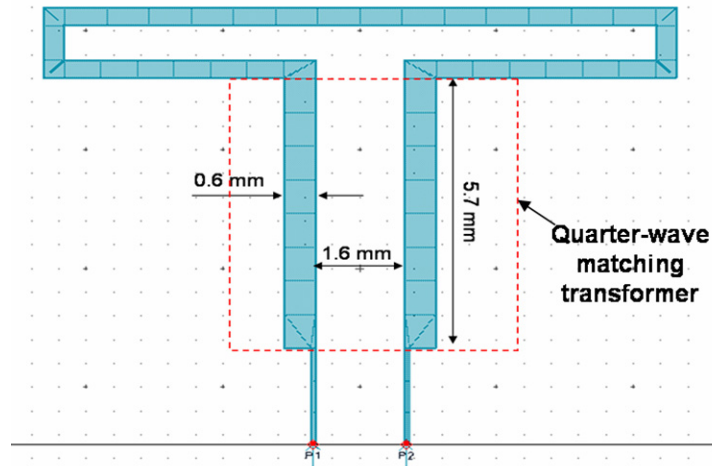

Figure 2.8 Folded-slot antenna with quarter-wave matching tranformer (Antenna Design parameters remain unchanged).

EM simulation of the folded slot antenna with the matching network has been carried out in ADS [22] and the results (return loss and input impedance characteristics) are shown in Figure 2.9. The matched folded slot antenna resonates at 10.2 GHz with a return loss of about 36 dB.

As a next step, a two-element folded slot antenna array has been designed for operation at 10 GHz and the details are discussed in the next section.

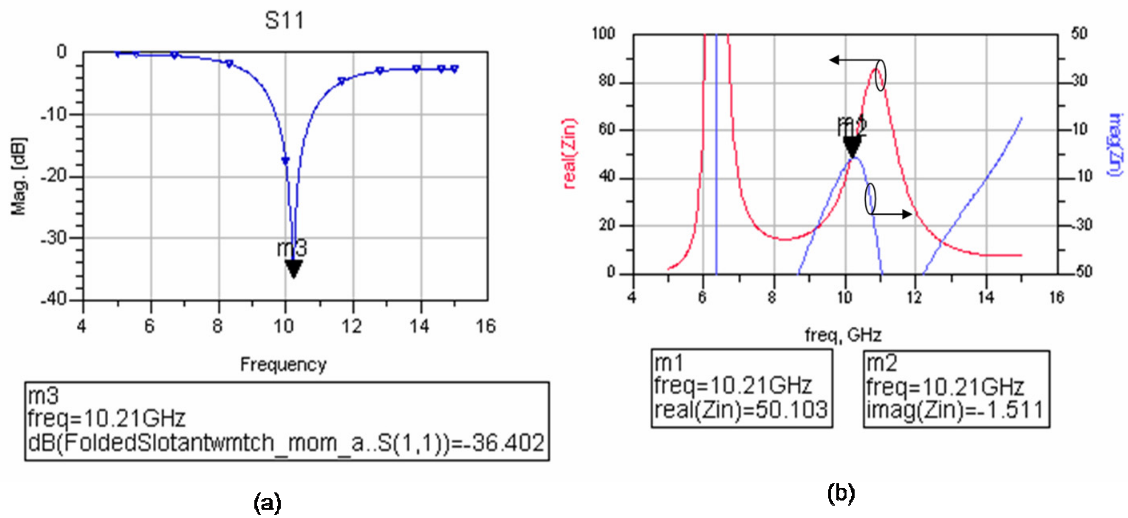

Figure 2.9. Performance of the matched folded slot antenna (a) Return loss, and (b) Real and Imaginary parts of the Input impedance.

2.4.2.4 Two Folded Slot Antenna Spaced 3λ/4 apart:

A two-element folded slot antenna array (shown in Figure 2.10) has been designed for operation at 10 GHz. The spacing between the antenna elements has been chosen to be S = 17.6 mm (~3λ_s/4 at 10 GHz).

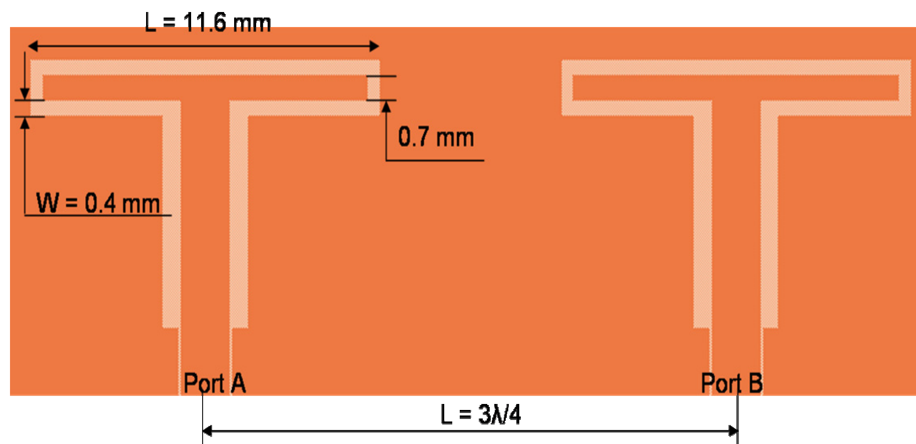

Figure 2.10. Two folded slot antennas placed 3λ/4 apart.

The two-element folded slot antenna array shown in Figure 2.10 has been simulated in ADS Momentum [22] and the return loss is shown in Figure 2.11. As expected, identical return loss performance was observed for both antenna elements.

2.4.2.5 Beam-steering Characteristics

The beam steering characteristics of the two-element antenna array for various phase shifts have been simulated using ADS. In these simulations, the input signal to Port B is phase shifted by Ø with Port A fed by zero phase shifted signal as shown in Figure 2.10. The beam angle of the two element antenna array in the H-plane for various phase shifts are shown in Figure 4.15, where Ø is the phase shift of the signal fed at Port B in Figure 2.10.

It can be observed that the beam angle changes from 0° to 19.5° as the phase shift of the signal fed at port P2 is changed from 0° to 90°. The beam steering angles for various phase shifts are summarized in Table 2.1. The expected beam steering angles for various phase shifts have been calculated using the standard formula [26]

$$\theta_0 = \cos^{-1}(-\phi / \beta d) \qquad (2)$$

where

θ_0 = direction of antenna beam.

ϕ = phase shift between the two antenna elements.

d = distance between the two antenna elements.

The beam steering angle in Table 2.1 is given by

$$\psi = 90^{\circ} - \theta_0 \qquad (3)$$

It can be noted that there is a good agreement between the beam steering angles obtained from the simulation and calculated using equations 2 and 3.

Table 2.1 Beam steering angle of the antenna array for various phase shifts (port P1 fed with zero phase shift signal and port P2 fed with phase shifted (Ø) signal).

Phase shift Ø at Port P2 (refer Figure 2.6)	Beam steering angle(ψ) (Using Formula in (1))	Beam steering angle(ψ) (EM Simulation)
0°	0°	0°
15°	3°	3°
30°	6°	6°
45°	10°	10°
60°	13°	13°
75°	16°	16°
90°	19.5°	19.5°

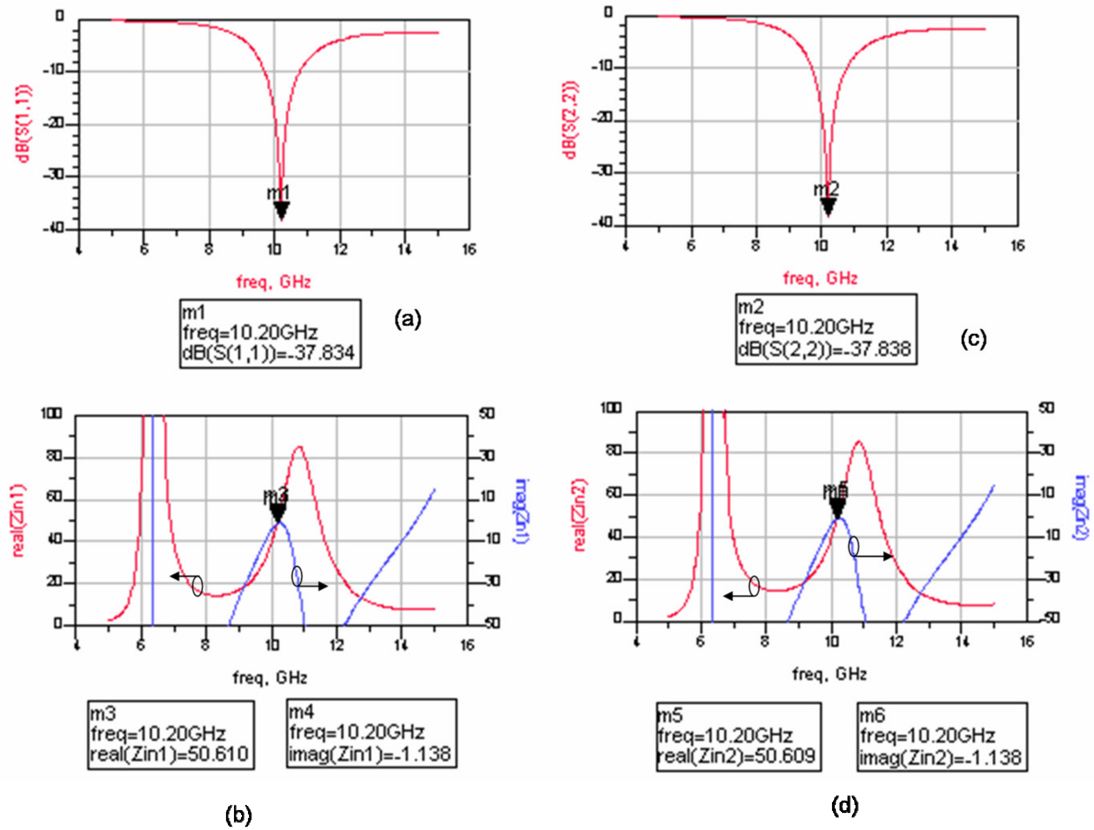

Figure 2.11.Performance of the two folded slot antenna spaced 3λ/4 apart. (a) and (b) present return loss and input Impedance data, respectively, for the slot antenna element on the left side in Figure 2.10, (c) and (d) present return loss and input Impedance data, respectively, for the slot antenna element on the right side in Figure 2.10.

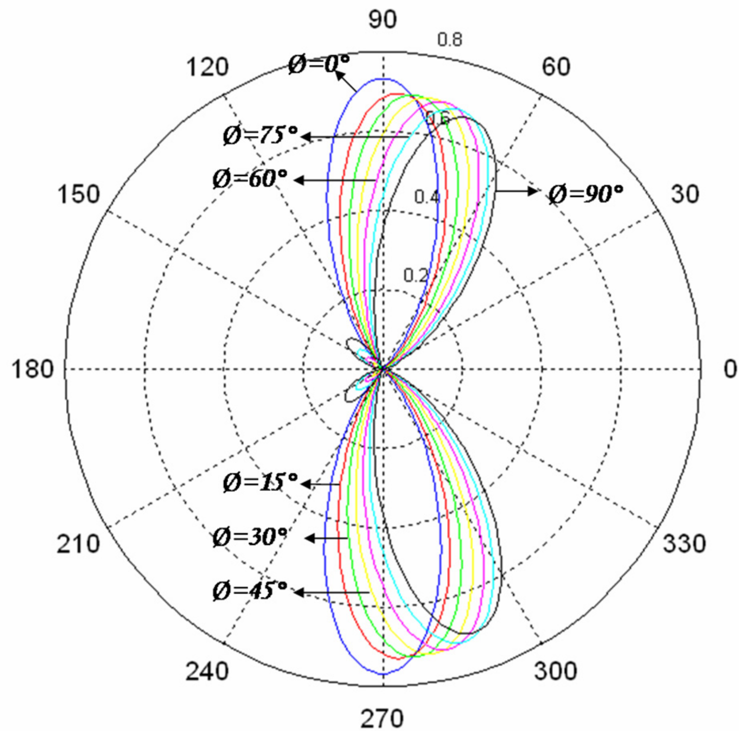

Figure 2.12. Simulated beam steering characteristics of the antenna array in the H-plane for various phase shifts (Port A fed with zero phase shifted signal and port Port B fed with the phase shifted signal (Ø) (Figure 2.10)).

In this chapter, design of the power divider and the antenna elements to be used in the MEMS ESA was discussed. Simulated performances of the power divider and the antenna elements have been presented. It has been shown that when the phase of one element in the antenna array is varied in steps of 15° to a total of 90°, the ESA beam can be steered by an angle of 20° away from the main beam direction. In the next chapter, design of the phase shifters that provide the required phase delays for steering the antenna beam will be discussed.

Chapter 3 PHASE SHIFTER DESIGN

In this chapter, design of 3 bit phase shifters to be used in the ESA will be discussed. Two types of phase shifters considered for use in the ESA, namely, Analog type RF-MEMS phase shifters and Digital type phase shifters (hereafter referred to as Bi-stable phase shifters) are described.

3.1 Analog type RF-MEMS Phase Shifters.

The ESA consists of two 3-bit phase shifters connected to antenna elements. Each 3-bit phase shifter has been designed by cascading three one-bit phase shifter units. A 3-bit phase shifter using the mainline type loaded line configuration was designed to provide the 3 phase bits, namely 15°, 30°, 45°. Loaded line phase shifters are based on the concept of loading a transmission line with two different impedances. This type of phase shifters with smaller bits can be cascaded to obtain multibit phase shifters.

In the analog type design, MEMS varactors are operated in two different states in the stable region. In the stable region, the air gap between the bottom electrode of the MEMS varactor and the CPW metallization (Figure 3.5(a)) can be controlled by changing the dc bias voltage. State 1 corresponds to the initial electrode position of the MEMS varactors at zero bias voltage. State 2 is achieved by applying a dc bias voltage (V_A) less than the pull-down voltage. The change in capacitance values obtained by operation in states 1 and 2 (in the stable region) provides the required phase shift. The two MEMS

varactors are connected to a common biasing circuit and hence the applied voltage is the same for both devices.

In the main line configuration shown in Figure 3.2, two identical MEMS shunt varactors are mounted directly on a main transmission line section of characteristic impedance Z_t and electrical length θ. Where θ is the electrical length of the physical spacing ℓ. MEMS varactors are operated in two different states in the stable region. State 1 corresponds to the initial electrode position of the MEMS varactors at zero bias voltage. State 2 is achieved by applying a dc bias voltage (V_A) less than the pull-down voltage. The change in capacitance values obtained by operation in states 1 and 2 (in the stable region) provides the required phase shift. The two MEMS varactors are connected to a common biasing circuit and hence the applied voltage is the same for both devices. The various phase bit values are obtained by changing the dc bias voltage applied to the MEMS varactors.

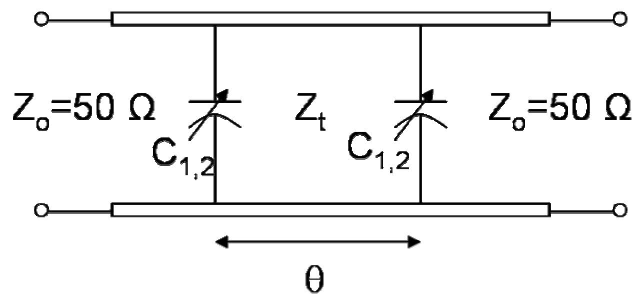

Figure 3.1 Schematic of a mainline type loaded line phase shifter.

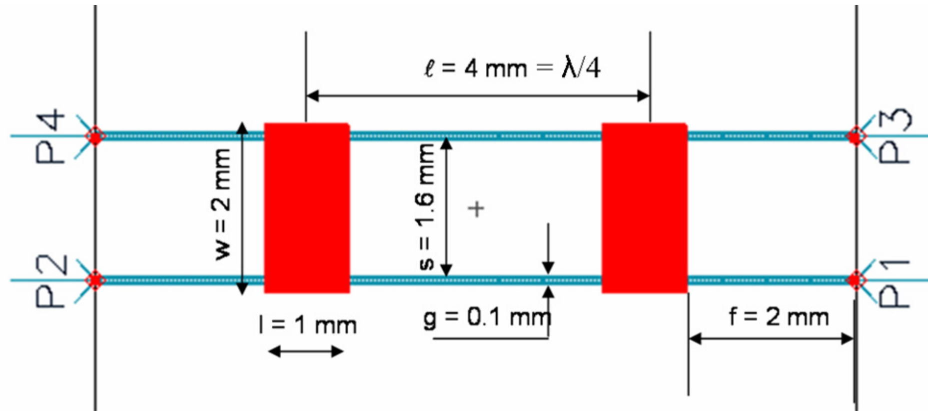

Figure 3.2 Layout of the loaded line type phase shifter with two MEMS varactors.

The length *l* and the width *w* of the MEMS top electrode are 1 mm and 2 mm, respectively. The up-position air gap height of the MEMS top electrode is 46.8 μm. BCB dielectric layer ($\varepsilon_r = 2.65$) of thickness 1 μm coated on the CPW line metallization is used to avoid electrical short between the electrodes.

The design parameters of the main transmission line section of the phase shifter shown in Fig. 6 are: Z_t =50 Ω and spacing ℓ = 4 mm (90° @ 13.6 GHz). To reduce the insertion loss of the phase shifter, the center-to-center spacing between the two MEMS varactors has been designed to be quarter-wavelength at a center frequency higher than the operating frequency range. The dimensions of the main CPW line are chosen to be *s* = 1.6 mm and g = 0.1 mm to provide Z_t =50 Ω on RT/Duroid 6002 substrate (ε_r = 2.94). The center conductor width and gap of the input/output 50 Ω CPW line sections (f = 2 mm in length) are 1.6 mm and 0.1 mm, respectively.

In order to get the desired phase shifts of 15°, 30° and 45°, the voltage applied to the varactors is changed. If the applied voltage is increased, the capacitance of the MEMS

varactor increases due to decrease in the gap height of the varactor and thus the phase shift provided by the phase shifter increases. The results from the EM simulation of the phase shifter are shown in Figure 3.3 and Figure 3.4.

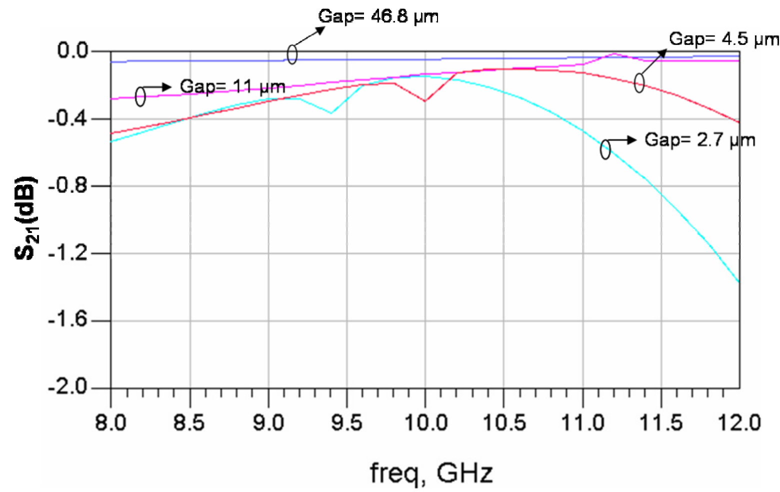

Figure 3.3. Phase shifter insertion loss for various gap heights.

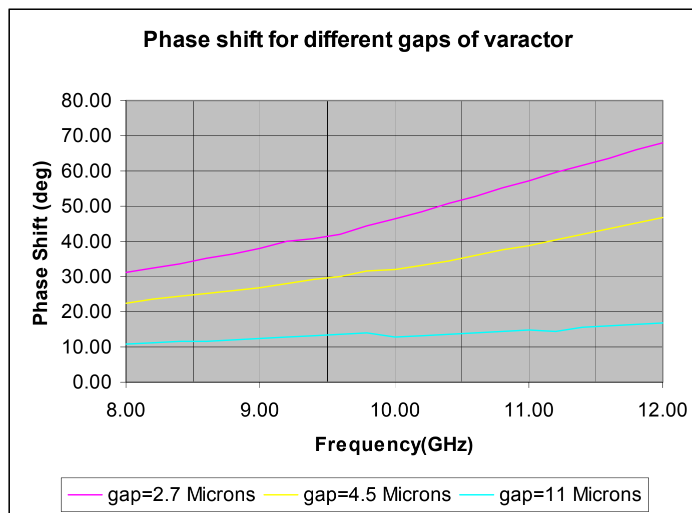

Figure 3.4. Phase shift corresponding to various gap heights of the MEMS varactors.

From the Figure 3.4, it can be seen that the phase shifter provides phase shift values of 15°, 30° and 45° when the gap height (between the movable plate and the CPW

metallization) of the MEMS varactors are 11, 4.5, and 2.7 µm, respectively. It can also be noted from Figure 3.3 that the maximum insertion loss is less than 0.3 dB for all the three cases. For practical applications, precise control of the applied voltage and hence the gap height is very difficult. Hence digital type of phase shifters were considered for operation in the ESA.

3.2 Bi-stable Varactor based phase Shifter design

In this section, 3-bit loaded line phase shifters using bi-stable MEMS varactors have been described. In the bi-stable design, MEMS varactors provide two different capacitance values corresponding to up position and down position of the membrane (Figure 3.5). In the down position, dc bias voltage is applied to pull down the membrane such that the bottom electrode is in contact with the dielectric layer. The phase shift depends on the difference between the two capacitance values provided by these two states. Bi-stable MEMS varactors have been designed to provide phase shifts of 15°, 30°, and 45°. In these designs, areas of the electrodes are changed to obtain the required capacitance. The thickness of the dielectric layer is same for all varactors.

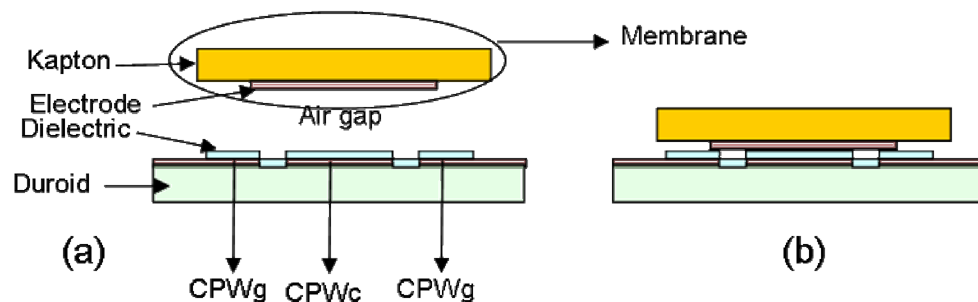

Figure 3.5. Cross section of bi-stable MEMS varactor in (a) up-state, (b) down-state.

3.2.1 Equivalent Circuit Model

A schematic model of the MEMS varactor with various capacitances between the varactor (bottom and top) electrodes and CPW conductors in the up-state are shown in Figure 3.6(a). A detailed equivalent circuit model for the MEMS varactor in the down-state is shown in Figure 3.6(b). This model can be simplified and represented as an equivalent shunt capacitance C_a across a transmission line as shown in Figure 3.6(c). Similarly, capacitance C_d can be obtained in the down state.

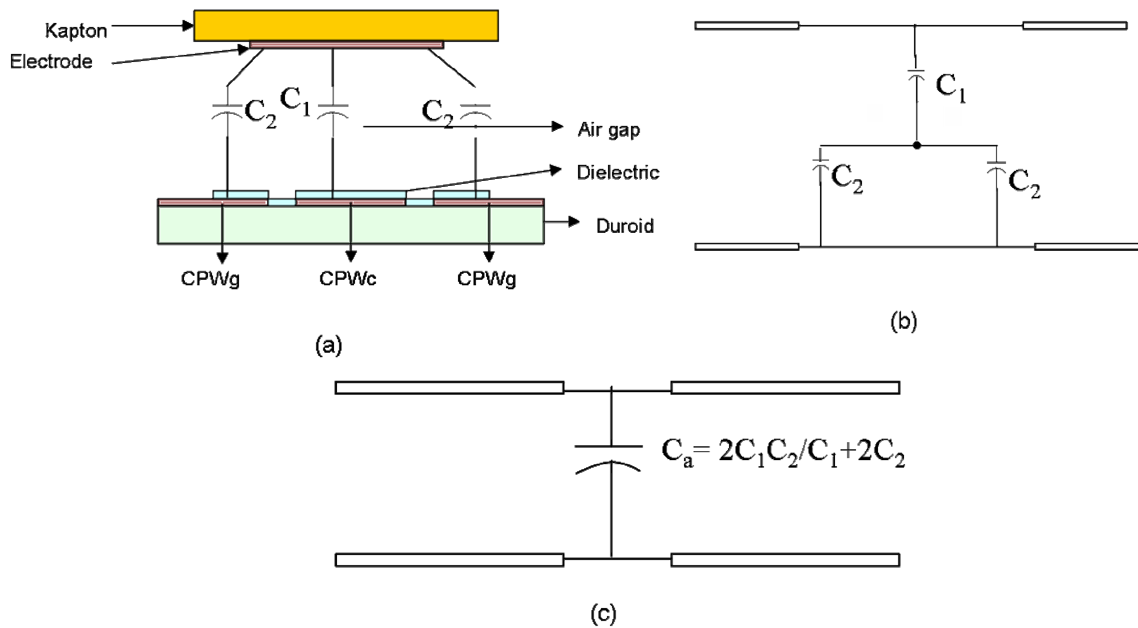

Figure 3.6. (a) Schematic of the MEMS varactor in up-state, (b) equivalent circuit model showing various capacitances and (c) equivalent circuit model with single equivalent capacitance.

The ESA consists of two 3-bit phase shifters connected to antenna elements. Each 3-bit phase shifter has been designed by cascading three one-bit phase shifter units. A one-bit phase shifter unit consists of two identical bi-stable MEMS varactors separated by

a center-to-center distance of quarter wavelength as indicated in Figure 3.2. In the bi-stable design, MEMS varactors provide two different capacitance values corresponding to the up position and down position of the MEMS varactor membrane. For operation, a DC bias voltage is applied to pull down the MEMS varactor membrane such that the top electrode is in contact with the dielectric layer (down position). The phase shift depends on the difference between the two capacitance values provided by these two states.

Top view of the bi-stable MEMS varactor is shown in Figure 3.7. The dimensions of the CPW line are chosen to be S = 1.6 mm and G = 0.1 mm to provide characteristic impedance Zt = 50 Ω on RT/Duroid 6002 substrate (ε_r = 2.94). The electrode dimensions of the MEMS varactor are: l_1 = 1 mm and w_1 = 2 mm. Dimensions l_2 and w_2 are varied to obtain the required capacitance and are listed in Table 3.1.The flexure design dimensions are: L_1=1.375 mm, L_2= 0.75 mm, L_3 = 1.375 mm, L_4 = 1 mm and the flexure width w = 0.2 mm. The thickness of the SU-8 dielectric layer (ε_r=4.2) is 14 μm. The design parameters and capacitance values obtained for various MEMS varactor designs using ANSOFT Q3D [27] are shown in Table 3.1. Insertion losses and phase delays obtained at 10 GHz from ADS Momentum simulations [22] for phase shifters implemented using these MEMS varactors are shown in Figure 3.8 and Figure 3.9, respectively.

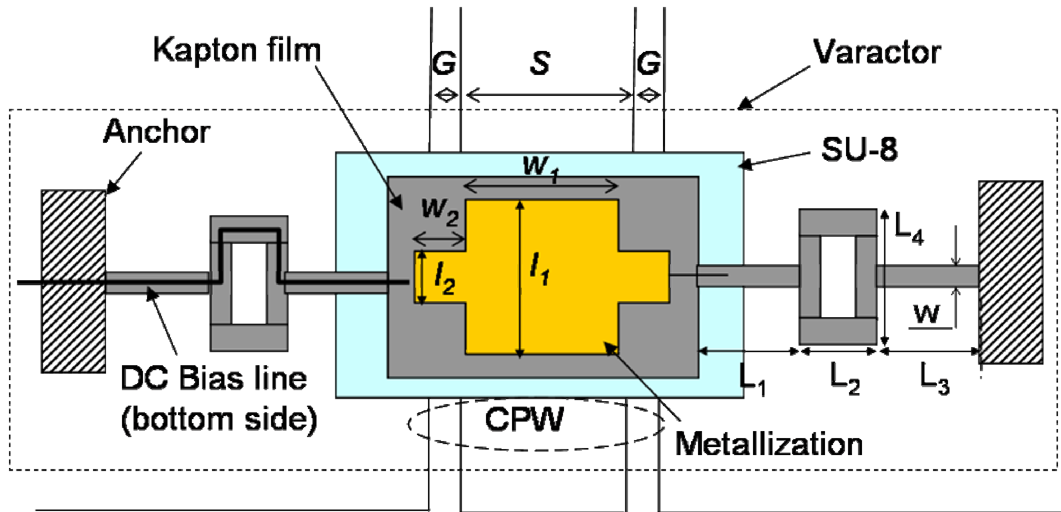

Figure 3.7. MEMS varactor top view (not to scale).

Table 3.1. Design parameters for the phase shifters with 14 um thick SU-8 used as the dielectric layer.

Phase shifter index	Up State Capacitance from (fF)	Down State Capacitance (fF)	w_2 (mm)	ℓ_2 (mm)	Phase shift @10 GHz Ø(deg)
1	70	167	0.1	0.1	16°
2	87	384	0.1	0.6	37°
3	119	784	0.15	1	81°

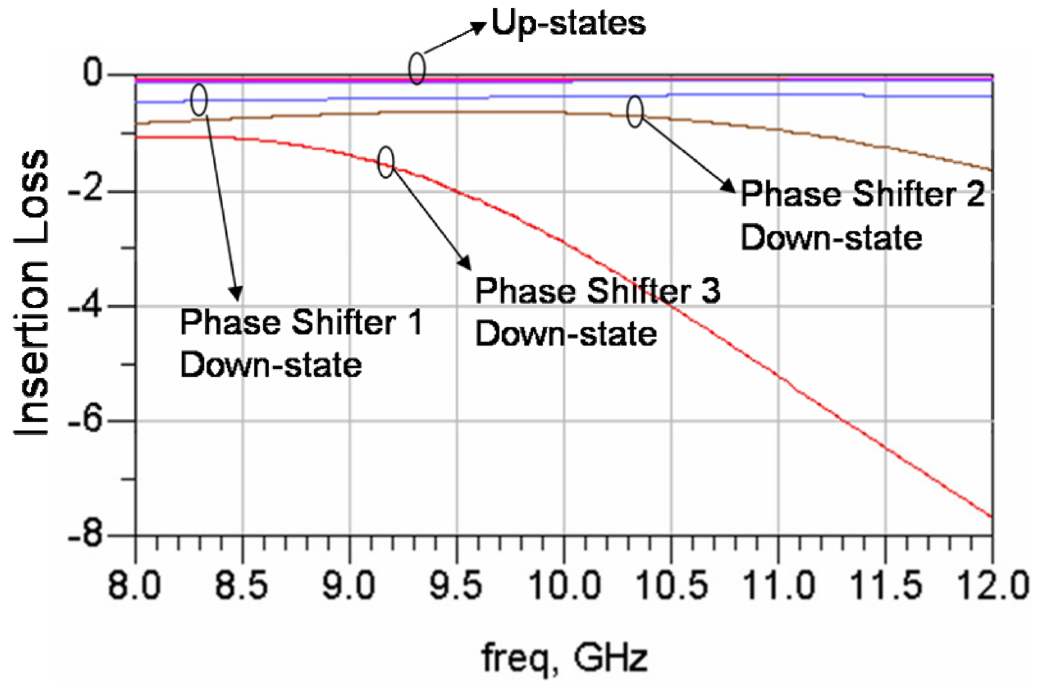

Figure 3.8. Insertion losses for various Bi-stable phase shifter units in the 3-bit phase shifter with 14 um thick SU-8 as the dielectric layer.

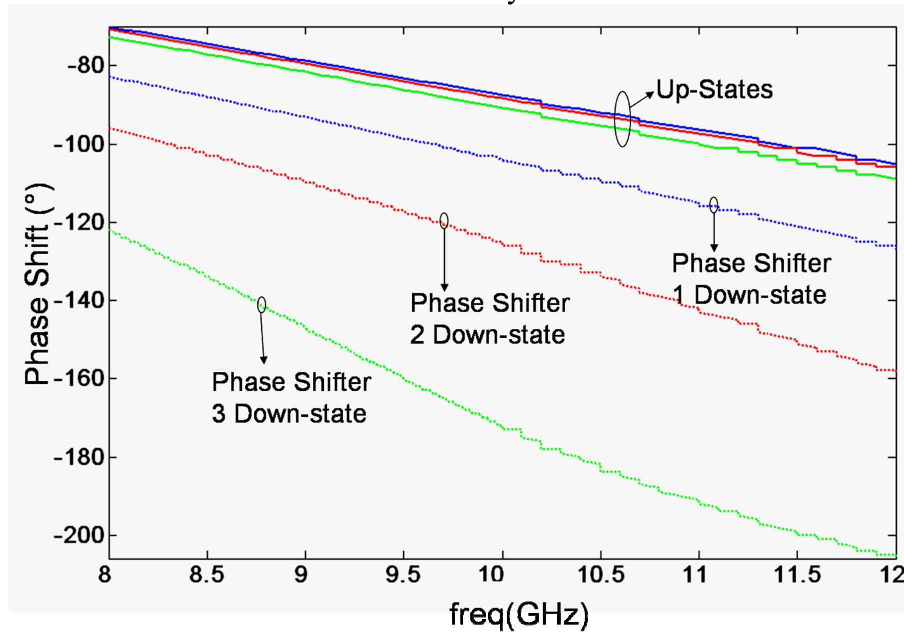

Figure 3.9. Phase delay for various Bi-stable phase shifter units in the 3-bit phase shifter with 14 um SU-8 as the dielectric layer.

From Figure 3.9, it can be seen that the phase shifters provide phase shift values of 15°, 30° and 45° respectively. It should also be noted from Figure 3.8 that the maximum insertion loss is about 4 dB for the 45° phase shifter unit. The reason for this is the high dielectric constant and loss tangent of the material SU-8 (ε_r=4.2, tan δ=0.08) used for these simulations. The insertion can be improved by using a low loss material like BCB (ε_r=2.65, tan δ=0.0012) as a dielectric. The varactors were simulated without changing the dimensions but with 12 um thick BCB as the dielectric layer and the corresponding change in capacitance and phase shift are listed in Table 3.2. Insertion loss and phase shift results with 12 um BCB as dielectric are shown in Figure 3.10 and Figure 4.15, respectively. It can be noted from these figures that the insertion loss could be incurred due to the higher dielectric constant of SU-8 is significantly reduced by using BCB as the dielectric material. Further, the phase shift also reduces significantly due the lower dielectric constant of BCB compared to SU-8.

Table 3.2. Design parameters for the phase shifters with 12 um thick BCB used as the dielectric layer.

Phase shifter index	Up State Capacitance from (fF)	Down State Capacitance (fF)	w_2 (mm)	ℓ_2 (mm)	Phase shift @10 GHz Ø(°)
1	66	141	0.1	0.1	10°
2	83	251	0.1	0.6	18°
3	110	427	0.15	1	22°

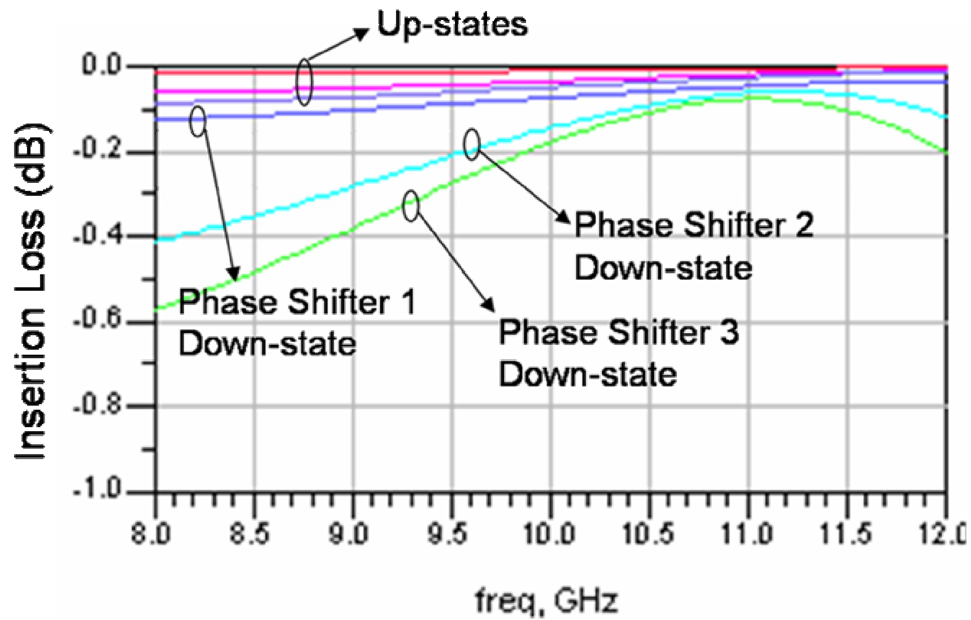

Figure 3.10. Insertion losses for various Bi-stable phase shifter units in the 3-bit phase shifter with 12 um thick BCB as the dielectric layer.

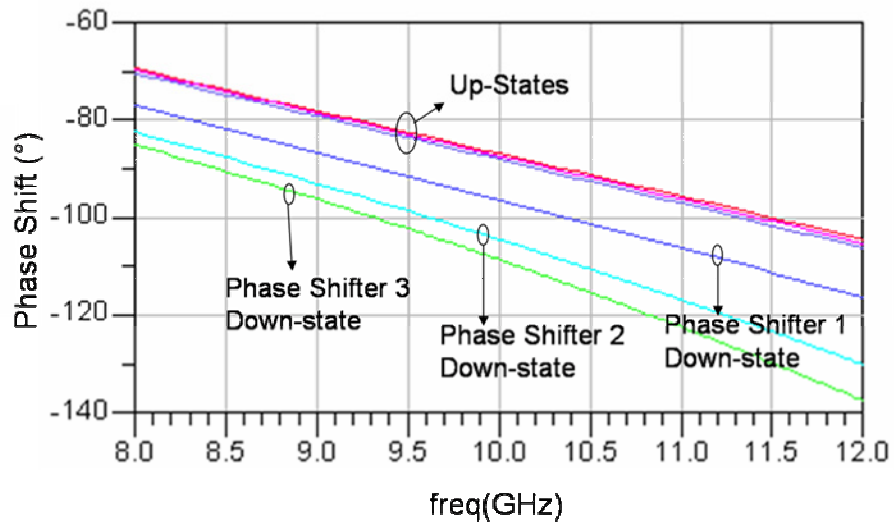

Figure 3.11. Phase delay for various Bi-stable phase shifter units in the 3-bit phase shifter with 12 um BCB used as the dielectric layer.

In this chapter, design of two types of phase shifters has been discussed. In chapter 2 and 3, the designs of various components of the ESA have been discussed. In the next chapter, fabrication, assembly and experimental characterization are discussed.

Chapter 4 FABRICATION AND EXPERIMENTAL CHARACTERIZATION

In the previous chapter, two design methodologies for phase shifter design were explained. In this chapter, ESA integrated with digital type MEMS phase shifters is discussed. Also, the fabrication procedure for the three layers and the thermo-compression bonding of the various layers used to obtain the integrated ESA will be explained.

4.1 Fabrication and Assembly

4.1.1 Substrate – CPW line:

The antenna structure is patterned on the 9 µm thick copper metallization on the RT/Duroid 6002 substrate. Figure 4.1 shows the patterned two-element slot antenna array on a 50 mm x 58 mm RT/Duroid 6002 substrate. Photosensitive BCB or SU-8 dielectric layer (Chapter #2) is spin-coated and patterned on the antenna metallization layer. In digital type bi-state MEMS phase shifters (discussed in Chapter 3), the MEMS electrode will make contact with the dielectric layer coated on the antenna metallization layer in the down position. Detailed processing steps are given in Appendix A of this thesis

.

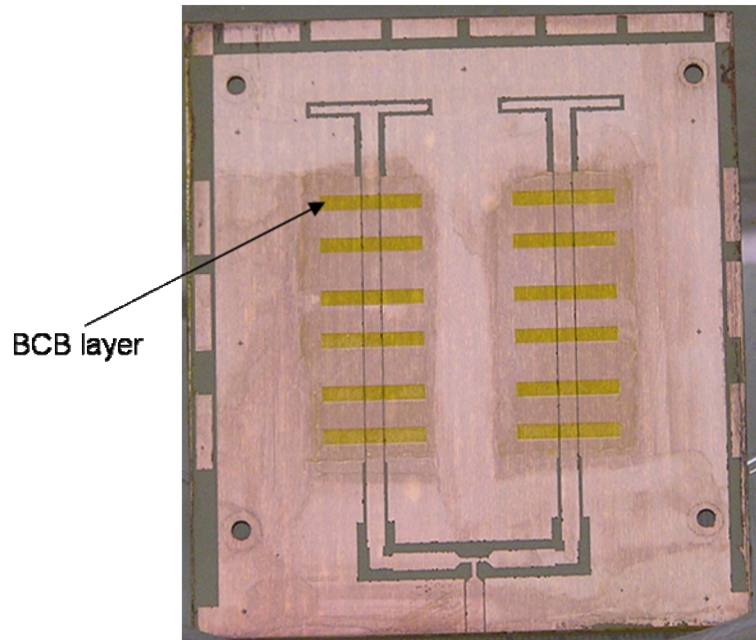

Figure 4.1 Antenna Pattern with BCB coating on RT/Duroid 6002.

Figure 4.2. Milled Bonding film.

4.2 Bonding film

The bonding film has been milled using CNC milling machine. A photograph of the milled bonding film is shown in Figure 4.2.

4.3 Kapton Film:

Kapton film pre-deposited with Nichrome (250 Å) and Copper (2 μm) is used in this project. The processing steps involved in the fabrication of the Kapton layer are described below.

1. MEMS varactor electrodes are patterned on the bottom side of the Kapton film by using the dummy mask and the actual mask as shown in Figure 4.3.

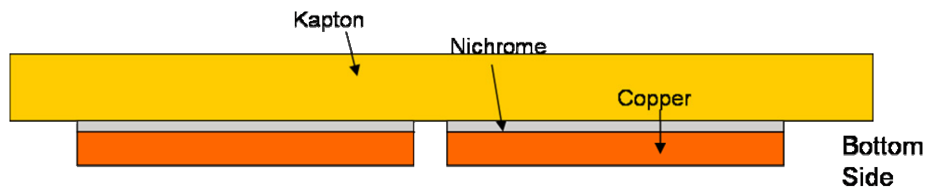

Figure 4.3. Bottom side of Kapton film after the use of dummy masks (not to scale).

2. Resistive Nichrome bias lines are defined by removing copper metallization at appropriate locations as shown in Figure 4.4.

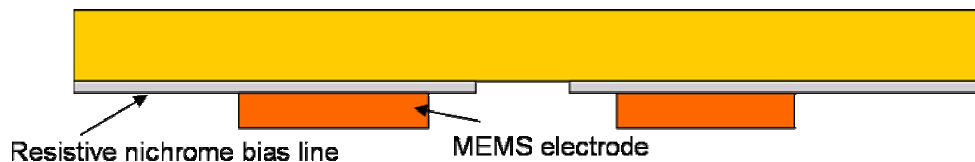

Figure 4.4. Kapton film with MEMS electrodes defined using actual mask (not to scale).

4.3.1 Machining the Kapton film:

In the past, excimer laser machining (services available from Photomachining Inc., http://www.photomachining.com/) was used for machining Kapton film. During the fabrication of the ESA, STS Multiplex Deep Reactive Ion Etching (DRIE) system available at Alabama Microelectronics science and Technology Center (AMSTC) was used for machining of the Kapton film. The steps in machining the Kapton film are described below.

Step 1: For the DRIE process, 0.5 μm thick aluminium mask layer is deposited on the Kapton film as shown in Figure 4.5.

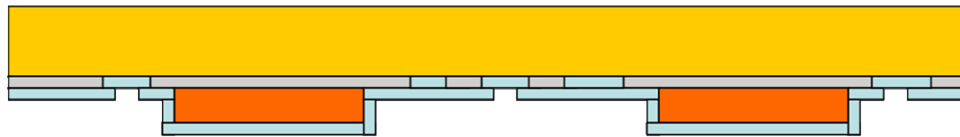

Figure 4.5. Aluminum mask layer on the Kapton for DRIE process (not to scale).

Step 2: The Kapton layer mask (shown in Figure 4.6) is aligned with respect to the alignment marks on the bottom layer of the Kapton film and the DRIE etch pattern is defined on the aluminium layer as shown in Figure 4.7.

Step 3: The Kapton layer is etched by DRIE process and the aluminum mask layer is etched off using 80% solution of Phosphoric acid. Cross sectional view of the Kapton layer after DRIE etching is shown in Figure 4.8. A photograph of the fabricated Kapton film is shown in Figure 4.9.

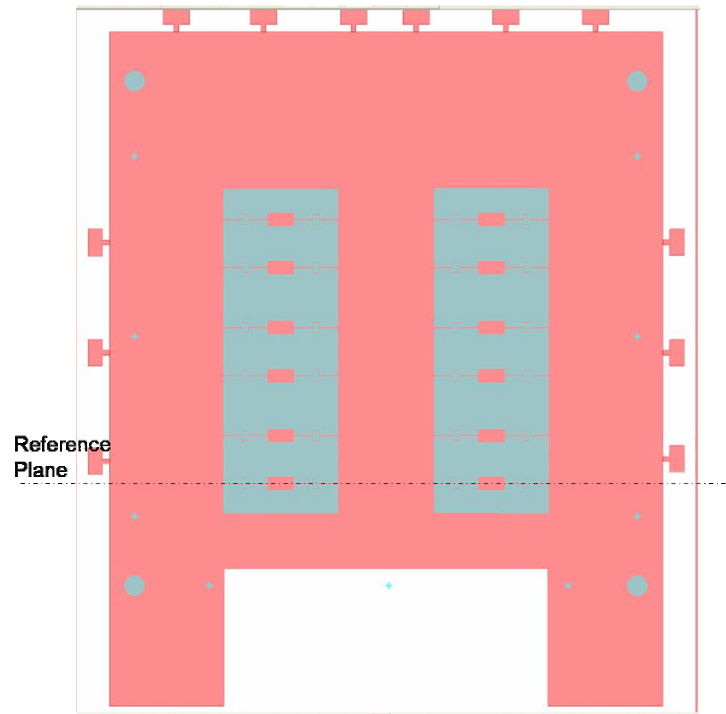

Figure 4.6. Kapton mask layer for DRIE Etching.

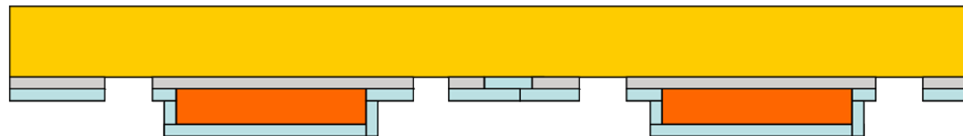

Figure 4.7. Cross section of Kapton showing patterned aluminum DRIE mask (not to scale).

Figure 4.8. Cross section of Kapton layer after DRIE (not to scale).

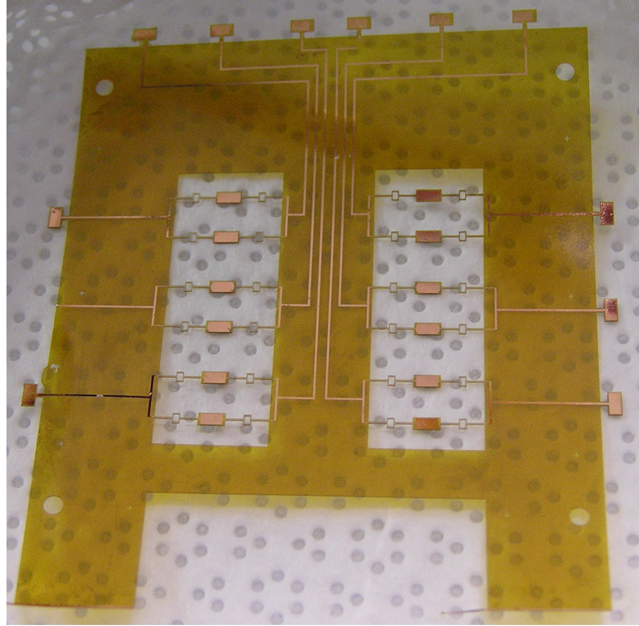

Figure 4.9. Kapton layer after the DRIE process.

4.4 Experimental Characterization

4.4.1 Fabrication Run #1:

A photograph of the fabricated Electronically Steerable Antenna with overall dimensions is shown in Figure 4.10. The measured return losses and the H-plane radiation patterns of the ESA are shown in Figure 4.11 and Figure 4.12, respectively. The return loss measurements have been carried out using an HP 8510C network analyzer. It can be observed from Figure 4.10 that the return loss of the ESA is 17 dB at the resonant frequency of 10.5 GHz for state 1 and 25 dB at 10 GHz for state 2. The antenna radiation patterns in two different states, shown in Figure 4.12, have been measured using Auburn University's pattern measurement system located in a 12m x 5m x 2.5m anechoic chamber. The *Beam 1* and *Beam 2* patterns correspond to zero phase shifted signal and

phase shifted signal, respectively, fed to the right antenna element in the two-element array. It can be seen from Figure 4.12 that the antenna beam shifts by 4° when the MEMS varactors in phase shifter units 2 and 3 (shown in Figure 4.10) are in the down state. Unfortunately, phase shifter unit 1 could not be actuated due to discontinuity in the resistive bias lines. The DC voltages required to pull down the MEMS varactors in the phase shifter units 2 and 3 are in the range of 160-170 V respectively. The estimated phase shift is 16° corresponding to the measured beam shift of 4°. The measured beam shift is lower than the expected value of 16° corresponding to a phase shift of 75°. The low phase shift value can be attributed to low capacitance ratio resulting from the surface roughness of the duroid substrate.

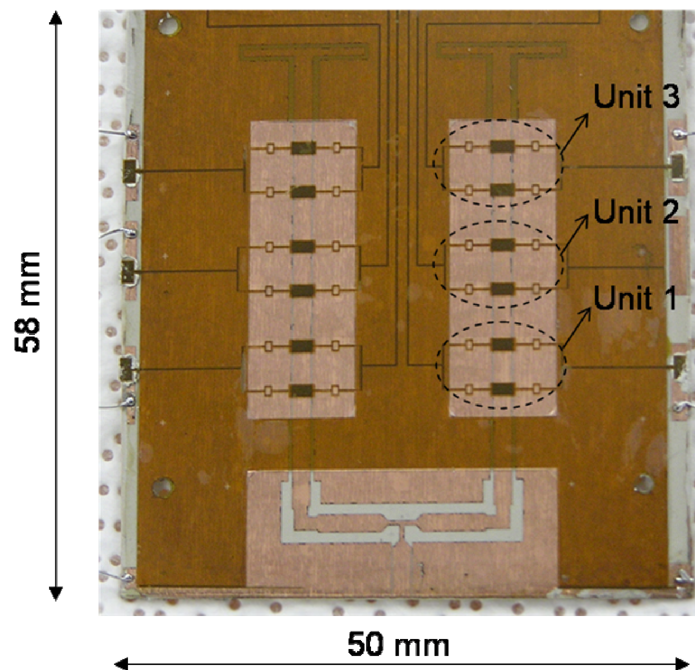

Figure 4.10. Fabricated Two-element X-band electronically steerable Antenna Prototype.

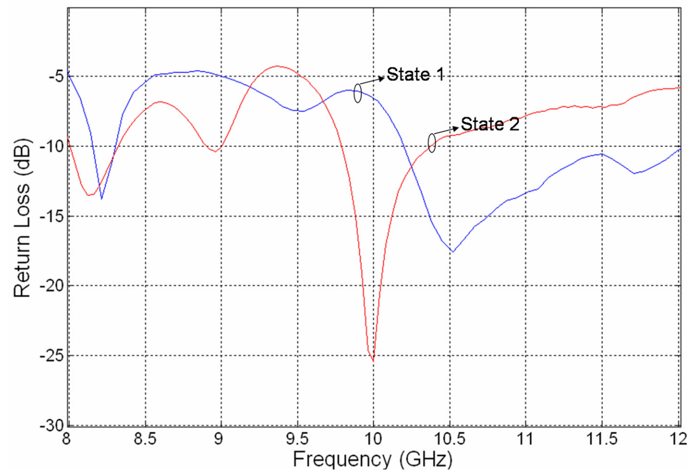

Figure 4.11. Measured return losses of the ESA prototype corresponding to two beam states.

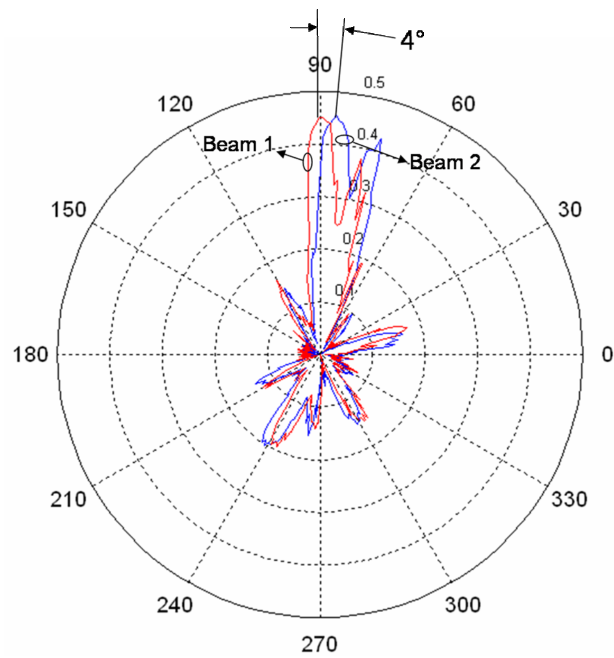

Figure 4.12. Antenna H-plane radiation patterns for the zero phase shifted signal (beam 1) and phase shifted signal (beam 2) fed to the right antenna element in the two-element array.

4.4.2 Fabrication Run #2:

In Run #2, the following improvements have been made to improve the overall antenna performance.

1. BCB dielectric layer is used instead of SU-8 dielectric layer to improve the insertion loss and the ESA radiated power. The loss tangent of BCB is 0.0012 @ 10 GHz whereas the loss tangent of SU-8 is 0.08 @ 1 MHz.
2. The power divider performance and hence the overall insertion loss of the antenna could be improved by using air bridges.

A photograph of the ESA fabricated in Run #2 with BCB dielectric layer and air bridges is shown in Figure 4.13. It has already been stated in the previous chapter that the use of BCB reduces the loss in the phase shifters. The simulated Insertion loss and the phase delays of the phase shifters with BCB dielectric layer are shown in Figure 4.14 and Figure 4.15. The expected beam shift of the ESA is 11° corresponding to a total phase shift of 50° (when all the MEMS varactors are down).

The measured return losses and the H-plane radiation patterns of the Run #2 ESA are shown in Figure 4.14 and Figure 4.15, respectively. It can be observed from Figure 4.14 that the return loss of the ESA is 33 dB at the operating frequency of 9.9 GHz in State 1 (all MEMS varactors in the up position) and 36 dB at the operating frequency of 9.5 GHz in State 2 (all MEMS varactors in down position). As expected, the operating frequency in state 2 is lower than that of state 1.

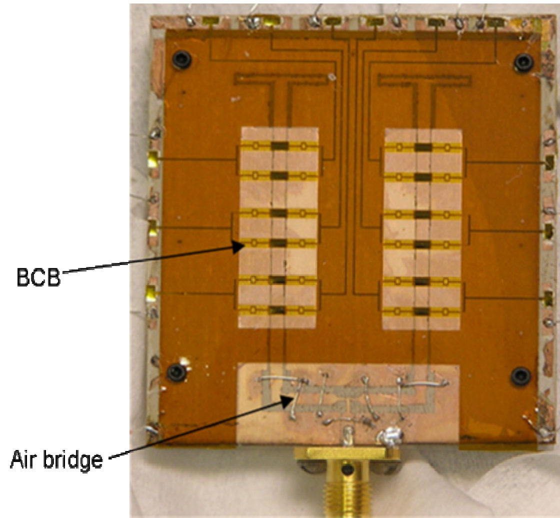

Figure 4.13. Photograph of the ESA fabricated in Run #2 with BCB dielectric layer and air bridges.

The antenna radiation patterns in two different states of the phase shifters, measured at 9.5 GHz are shown in Figure 4.15. The radiation patterns in state 1 and state 2 correspond to zero phase shift signal and phase shifted signal, respectively, fed to the right antenna element in the two-element array. The DC voltages required to pull down various MEMS varactors in the phase shifter are in the range 110-150 V. The beam shift between the pattern peaks in state 1 and state 2 is 8°. The half-power beam widths in state 1 and state 2 are 37° and 51°, respectively. If the main beam direction for each state was chosen to be the line passing through the center of the half-power beam width, the main beam direction in state 2 shifts 16° with respect to state 1.

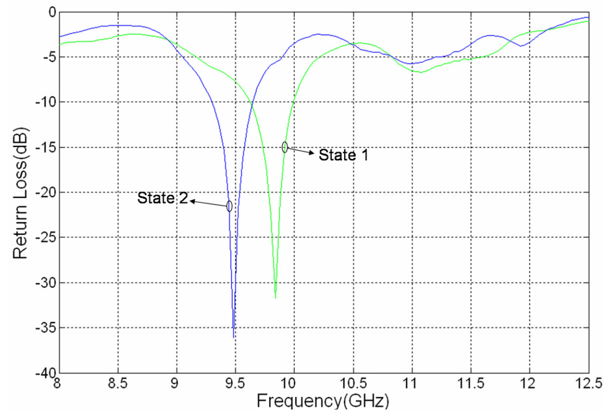

Figure 4.14. Measured return loss for the ESA prototype from Run #2 with a) State 1 when all MEMS varactors in up position corresponding to zero phase shift condition, and b) State 2 when all MEMS varactors on the left side are in the down position.

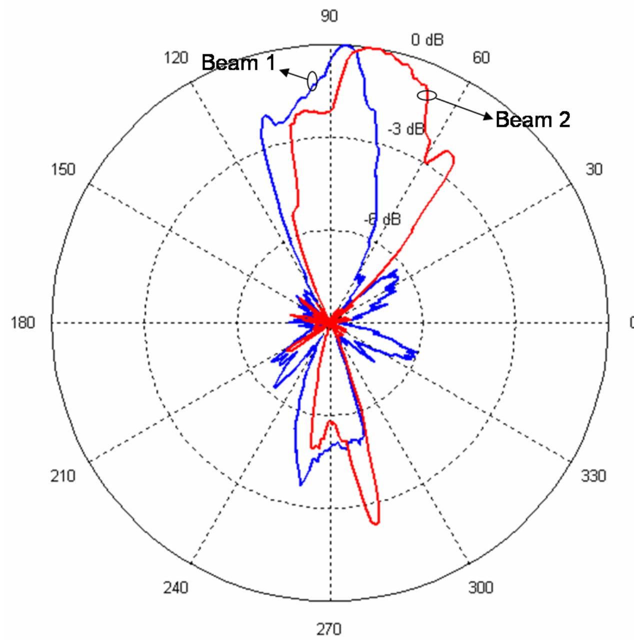

Figure 4.15. Antenna H-plane measured radiation patterns for the zero phase shifted signal (beam 1) and phase shifted signal (beam 2) fed to the right antenna element in the two-element array.

4.4.3 Fabrication Run #3

Since the fabrication process in Run #1 and Run #2 did not result in all MEMS devices' actuation mainly due to removal of aluminum used as a masking material, for fabrication Run#3, it was decided that the top layer of Kapton film will be sent out for laser cutting. All the other fabrication details were the same as in Fabrication Run #2. The return loss results obtained from the Antenna structure fabricated with the Kapton film obtained from Laser cutting are shown in Figure 4.16 and Figure 4.17. It can be observed from Figure 4.16 that the return loss of the ESA is 55 dB at the operating frequency of 9.1 GHz in State 1 or up-state (all MEMS varactors in the up position) and ranges from 23 dB to 35 dB with the 15˚ phase shifter in the down state and the 45˚ phase shifter down at an operating frequency range of 9.05 GHz to 9.09 GHz. The return loss provided by the antenna in State 2 (all MEMS varactors in down position) is again 23 dB. As expected, the operating frequency in state 2 is lower than that of state 1. The DC voltages required to pull down various MEMS varactors in the phase shifter are in the range 140 - 215 V.

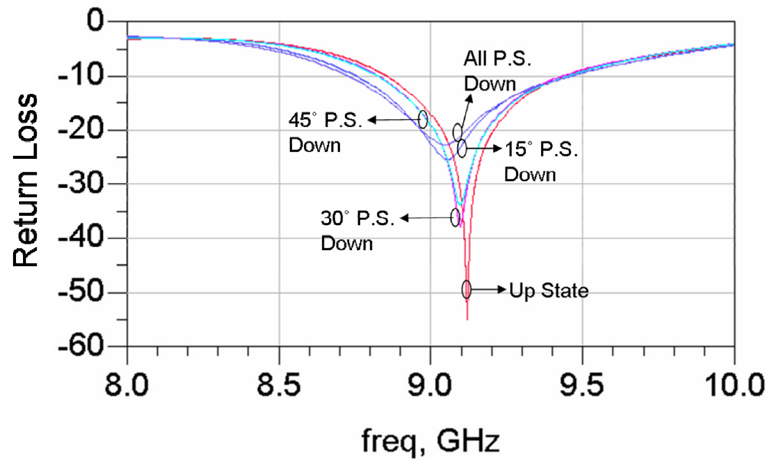

Figure 4.16 Measured return loss for the ESA prototype from Run #3 with up-state and states with different MEMS phase shifters actuated from the left side of the Antenna array.

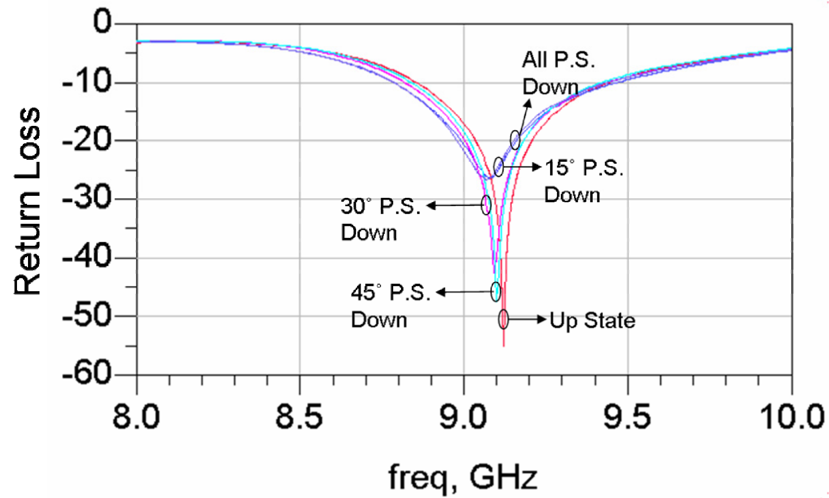

Figure 4.17. Measured return loss for the ESA prototype from Run #3 with up-state and states with different MEMS phase shifters actuated from the right side of the Antenna array.

It can be observed from Figure 4.17 that the results obtained from the actuation of the MEMS phase shifters on the right side of the antenna array match very closely with

those obtained from the actuation of the devices from the left side of the antenna array. Figure 4.18 shows the measured radiation pattern for the ESA from Fabrication Run #3. When the right side phase shifter Units #1, #2 and #3 (shown in Figure 4.10) are actuated, the ESA provides beam steering angles of 5˚, 15˚ and 18˚, respectively. It can also be seen that the ESA provides a peak-to-peak beam steering angle of 20˚ when all the phase shifters are actuated at the same time as shown in Figure 4.18.

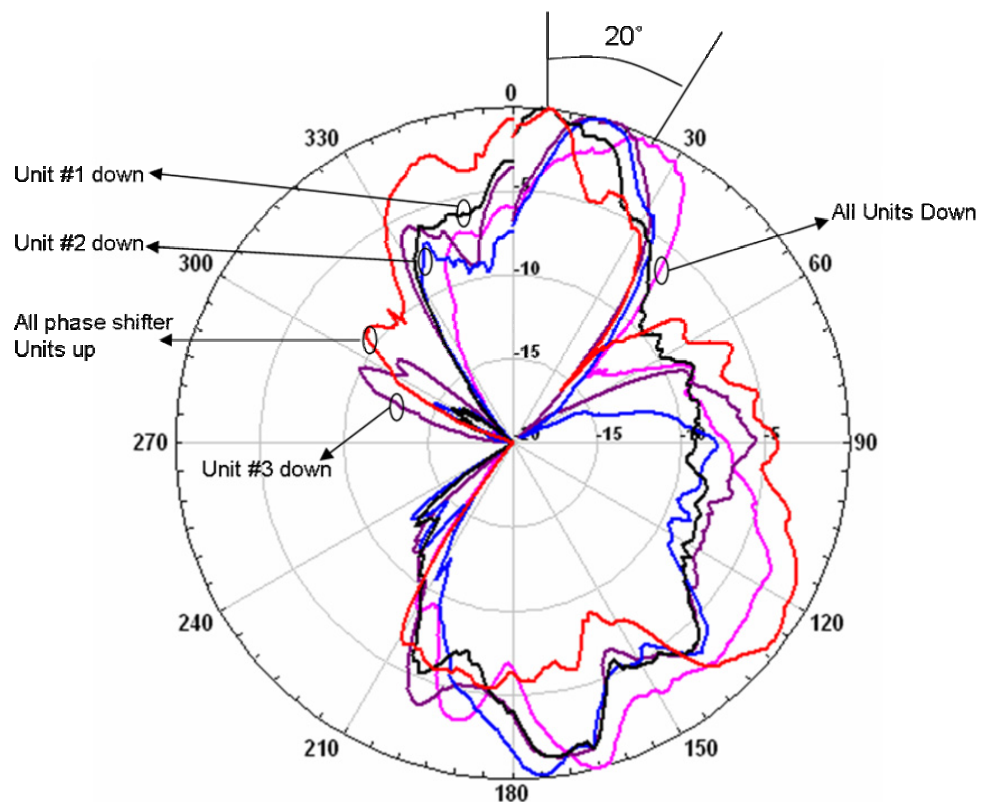

Figure 4.18. ESA #3 H-Plane radiation pattern with different phase shifters actuated. Phase shifter Units #1, #2 and #3 have been illustrated in Figure 4.10.

Chapter 5 SUMMARY AND FUTURE WORK

5.1 Summary

An approach for cost effective fabrication and assembly of Electronically Steerable Antenna arrays has been presented in this thesis. The MEMS phase shifters used in the antenna array are fabricated using Flexible Printed Circuit (FPC) technology (referred as FlexMEMS). The dimensions of the MEMS phase shifters are of the order of mils. The advantages of this approach include low cost, high volume fabrication, and integration with printed circuit electronics. The use of printed circuit processing enables ease of integration of MEMS devices with associated control electronics and fabrication of complex multi-layer 3D structures.

5.2 Design

A folded slot antenna design has been used in this thesis to implement the antenna elements of the ESA owing to the reduced input impedance characteristics of this type of design. The folded slot antenna design provides a return loss of 35 dB at a frequency of 10 GHz. It has also been shown that when the phase of one element in the antenna array is varied in steps of 15° to a total of 90°, the antenna array beam can be steered by an angle of 20° at the frequency of 10 GHz. To obtain the required phase difference, designs of phase shifters providing 15°, 30° and 45° of phase shift in two configurations namely, the analog type design and the digital type design has been described. Digital type of

phase shifters was chosen to be integrated with the ESA owing to the difficulty in precisely controlling the operation of the analog type phase shifters.

5.3 Fabrication and Assembly

The fabrication of the three different layers of the ESA was discussed and presented. Further details of the fabrication process are listed in Appendix A of this thesis. The substrate layer for the ESA that consists of the antenna elements and power divider is fabricated using conventional lithography techniques. A polyflon film used as a spacer layer between the substrate and the electrodes of the phase shifters has been machined by a vertical mill. The top layer for the MEMS electrodes have been fabricated using conventional lithography techniques. These three layers are bonded to get the final ESA structure using thermo-compression bonding at a pressure of 65 psi and at 130 °C.

5.4 Experimental Characterization

Experimental results for the fabricated ESA have been presented showing an antenna beam steering angle of about 20° for a simulated phase shift of 50° provided by the phase shifters.

5.5 Future Work

An antenna array using monolithic integration of RF MEMS phase shifters with Antenna elements has been presented in this thesis. Reliability of these types of devices has been performed for 1 million cycles has already been presented in [26]. In this section, suggestions for future improvements of the ESA characteristics are discussed.

The copper metallization on the Duroid substrate layer has a surface roughness of 1-2 μm which leads to an increase in the loss characteristics and also a decrease in the

capacitance ratio obtained in the two states of operation of the MEMS varactor. The surface roughness of the Duroid substrate could be reduced by chemical mechanical polishing to improve the capacitance ratio and hence the phase shift and the corresponding beam shift of the antenna.

Since polyimide has high water moisture absorption, typically 1-3 percent water absorption by weight, polyimide films tend to curl and blister under the metallization, which in turn changes the electrical performance of the circuit. On the other hand, Liquid crystal polymer (LCP) has low moisture absorption (0.04-0.1 percent), low dielectric constant, low loss, stable electrical properties over humidity, high temperature stability and high mechanical strength. Because of these properties, LCP is most suitable for high volume and low cost packaging of FlexMEMS [29] based phase shifters. Since electrical properties of LCP are very similar to those of Kapton polyimide films, the ESA design presented in this thesis could be fabricated and packaged using multi-layer LCP construction (substrate, spacer, membrane layer and packaging layers).

BIBLIOGRAPHY

[1] "Affordable Phase Shifters", Agile Materials and Technologies, www.agilematerials.com.

[2] S. Cass, "Large Jobs for little devices", IEEE Spectrum, Vol. 38, Issue 1, pp. 72-73.

[3] T. Ohira and K. Gyoda, "Electronically Steerable Passive Array Radiator Antennas for Low-Cost Analog Adaptive Beamforming", IEEE International Conference on Phased Array Systems and Technology, 21-25 May 2000, pp. 101-104.

[4] http://www.memtronics.com

[5] S. Lucyszyn, "Review of radio frequency microelectromechanical systems technology", IEE Proceedings on Science, Measurement and Technology, Vol. 151, Issue 2, pp. 93-103.

[6] C. L. Goldsmith, Z. Yao, S. Eshelman, and D. Denniston, "Performance of low-loss RF MEMS capacitive switches," IEEE Microwave Guided Wave Lett., vol. 8, pp. 269–271, Aug. 1998.

[7] D. Hyman, J. Lam, B. Warneke, A. Schmitz, T. Y. Hsu, J. Brown, J. Schaffner, A. Walston, R. Y. Loo, M. Mehregany, and J. Leen, "Surface- micromachined RF MEMS switches on GaAs substrates," Int. J. RF Microwave CAE, vol. 9, no. 4, pp. 348–361, Aug. 1999.

[8] G. M. Rebeiz and J. B. Muldavin, "RF MEMS switches and switch circuits," IEEE Microwave Mag., pp. 59–71, Dec. 2001.

[9] J. J. Yao, "RF MEMS from a device perspective," J. Micromech. Microeng., vol. 10, no. 4, pp. R9–R38, 2000.

[10] A. Dec and K. Suyama, "Micromachined electro-mechanically tunable capacitors and their applications to RF IC's," IEEE Trans. Microwave Theory Tech., vol. 46, pp. 2587–2596, Dec. 1998.

[11] C. L. Goldsmith, A. Malczewski, Z. J. Yao, S. Chen, J. Ehmke, and D.H. Hinzel, "RF MEMs variable capacitors for tunable filters," Int. J. RF Microwave CAE, vol. 9, no. 4, pp. 362–374, Aug. 1999.

[12] N. Hoivik, M. A. Michalicek, Y. C. Lee, K. C. Gupta, and V. M. Bright, "Digitally controllable variable high-Q MEMS capacitor for RF applications," in IEEE MTT-S Int. Microwave Symp. Dig., May 2001, pp. 2115–2118.

[13] N. S. Barker and G. M. Rebeiz, "Distributed MEMS true-time delay phase shifters and wide band switches," IEEE Trans. Microwave Theory Tech., vol. 46, pp. 1881–1890, Nov. 1998.

[14] B. Pillans, S. Eshelman, A. Malczewski, J. Ehmke, and C. Goldsmith, "K-band 3-bit low-loss distributed MEMS phase shifter," IEEE Microwave Guided Wave Lett., vol. 9, pp. 520–522, Dec. 1999.

[15] M. Kim, J. B. Hacker, R. E. Mihailovich, and J. F. DeNatale, A DC-to-40 GHz Four-Bit RF MEMS True-Time Delay Network, vol. 11, no. 2, pp. 56–58, Feb. 2001.

[16] G. M. Rebeiz, G.-L. Tan, and J. S. Hayden, "RF MEMS phase shifters: design and applications," IEEE Microwave Magazine, pp. 72–81, June 2002.

[17] H.-T. Kim, J.-H. Park, Y.-K. Kim, and Y. Kwon, "Millimeter-wave micromachined tunable filters," in IEEE MTT-S Int. Microwave Symp. Dig., vol. 3, 1999, pp. 1235–1238.

[18] D. Peroulis, S. Pacheco, K. Sarabandi, and L. P. B. Katehi, "Tunable lumped components with applications to reconfigurable MEMS filters," in IEEE MTT-S Int. Microwave Symp. Dig., vol. 3, May 2001, pp. 341–344.

[19] J. Brank, J.Yao, M. Eberly,A. Malczewski, K.Varian, and C. Goldsmith, "RF MEMS-based tunable filters," Int. J. RF Microwave CAE, vol. 11, no. 5, pp. 276–284, Aug. 2001.

[20] Y. Liu, A. Borgioli, A. S. Nagra, and R. A. York, "Distributed MEMS transmission lines for tunable filter application," Int. J. RF Microwave CAE, vol. 11, no. 5, pp. 254–260, Aug. 2001.

[21] R. Ramadoss, A.Sundaram, and Lucas Feldner, "RF MEMS Phase Shifters based on PCB MEMS Technology," IEE Electronic Letters, Vol. 41, Issue 11, pp. 654-656.

[22] ADS Momentum, available from Agilent Technologies, www.agilent.com.

[23] T.M. Weller, R.M. Henderson, K.J. Herrick, S.V. Robertson, R.T. Kihm, and L.P.B. Katehi, “Three-dimensional high-frequency distribution networks. I. Optimization of CPW discontinuities,” IEEE Trans. on Microwave Theory and Tech., Vol. 48, no. 10, Oct. 2000 pp.1635–1642.

[24] H.Tsai, Robert A. York, “FDTD Analysis of CPW-Fed Folded-Slot and Multiple-Slot Antennas on Thin Substrates”, IEEE Transactions on Antennas and Propagation, Vol.44, No.2, pp 217-226, Feb 1996.

[25] Microwave Engineering by David M. Pozar.

[26] Antenna Theory and Design by W.L. Stutzman and G.A. Thiele.

[27] Ansoft Q3D Extractor and Ansoft HFSS, available from Ansoft Corporation, www.ansoft.com.

[28] R. Ramadoss, S. Lee, K. C. Gupta, Y. C. Lee, and V. M. Bright, “Fabrication, Assembly, and Testing of RF MEMS capacitive switches using flexible printed circuit technology,” *IEEE Transactions on Advanced Packaging,* vol. 26, no. 3, August 2003, pp. 248-254.

[29] “Design, Modeling, and Characterization of RF MEMS Capacitive Switches based on Flexible Printed Circuit Technology”, Ramesh Ramadoss, University of Colorado.

[30] “Fractal Shaped Antenna Elements for Wide and Multi-Band Wireless Applications”, K.J.Vinoy, Penn State Univerity, 2002.

[31] “Fractal Antennas: Design, Characterization and Applications”, John Gianvittorio, UCLA, 2000.

[32] Rainee N. Simons, “Coplanar Waveguide Circuits, Components and Systems,” Wiley Series in Microwave and Optical Engineering.

APPENDICES

Appendix A FABRICATION AND PROCESSING DETAILS

A.1 Fabrication and Processing Details

The sequential steps involved in the fabrication and assembly of polyimide film based RF MEMS switches are shown in Figure A.1. The design details for the antenna and the phase shifters are discussed in previous chapters. The fabrication and processing details are discussed in the following sections.

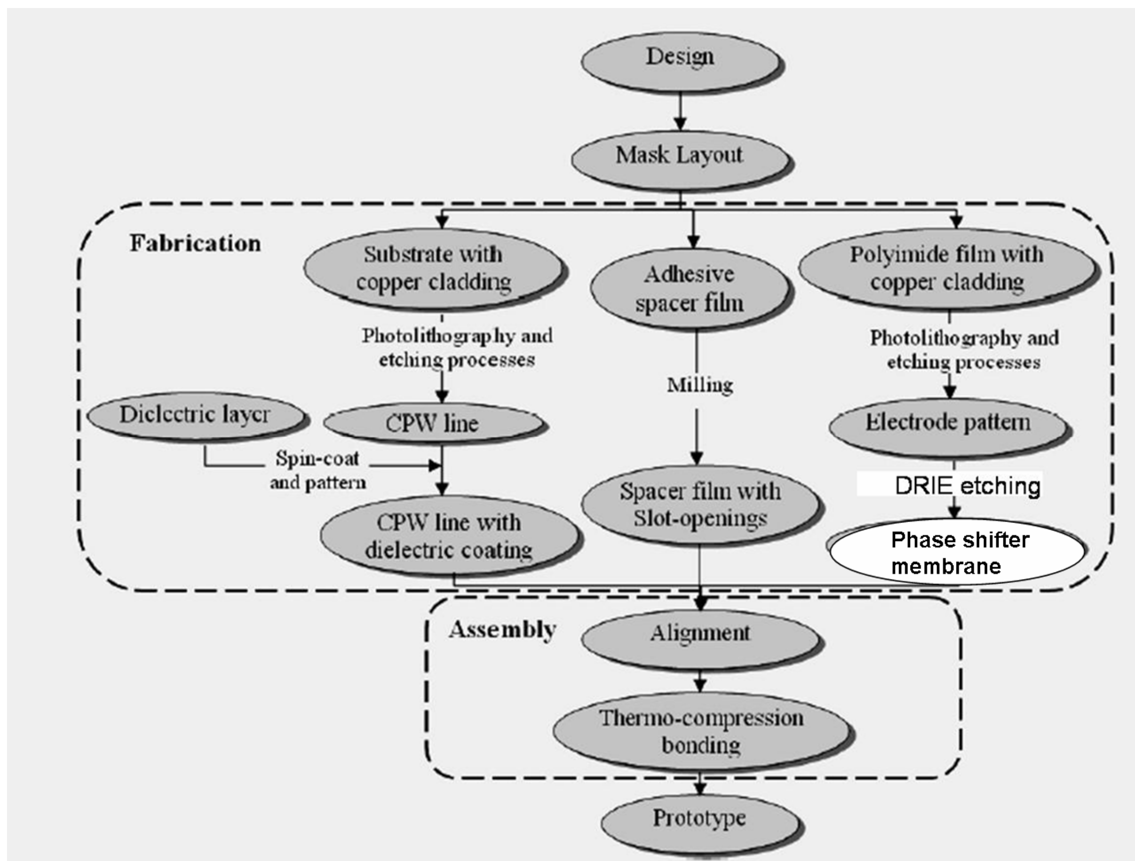

Figure A.1 Fabrication Steps and flow.

A.2 Layout Creation

The various layers of the ESA such as the CPW line, dielectric coating layer, machining pattern in 'adhesive spacer film' layer, phase shifter top electrode pattern, and the DRIE etching pattern in the Kapton polyimide film layer are drawn in AutoCAD.

Then, these layers are copied onto a single layer. For mask printing (at Infinite Graphics, Inc., MN), the features are drawn in two layers i) paint layer - containing the pattern to be printed, ii) scratch layer - containing the pattern to be removed from the paint layer. For example, to generate a rectangular ring pattern a big rectangle is drawn in the paint layer and a small rectangle is drawn in the scratch layer.

A.3 Glass Mask Preparation

A glass mask is a square glass plate that contains a photoresist layer on top a chromium layer on one side. A glass "photomask" is created by transferring the pattern from the mask film to the glass mask by photolithography.

A.4 Substrate Layer

In this section, details of substrate preparation and pattern definition are described.

A.4.1 Machining and Drilling

Four alignment holes of size 1/16" are drilled in the substrate and the substrate is machined to the required size. Drilling and machining of the substrate are done using a vertical mill.

A.4.2 Defining Pattern

The required patterns are defined by photolithography and etching processes.

A.4.2.1 Photolithography

The term 'Photolithography' refers to the process of defining geometric shapes on the surface of a substrate with the aid of light (typically using Ultra Violent light). The typical steps involved in the photolithographic process are photoresist application, soft baking, mask alignment, exposure and development, and hard-baking.

(1) Surface cleaning: The transparent protective film (self-adhering polyethylene sheet) present on the both sides of substrate is removed. Adhesive dicing film ("Blue Medium Tack Squares", available from Semiconductor Equipment Corp.,CA) is used to protect the bottom side of the sample and the sample is placed on the spinner 1.5" chuck). The spinner is spun at a speed of 2000 rpm to 2500 rpm and the surface is chemically cleaned using acetone and methanol sprayed simultaneously on the surface for approx 1 min. This step helps remove any adhesive residue left on the surface as well as any traces of organic, ionic, or metallic impurities.

(2) Photoresist application: Photoresist S1813 (available from Microchem Inc., MA), a positive photoresist is used in this project. In positive photoresists, wherever the resist is exposed to the UV light will dissolve in the developer (CD-30). Therefore, the mask contains an exact copy of the pattern to be defined on the substrate. Exposure to the UV light changes the chemical structure of the resist so that it becomes soluble in the developer. The exposed resist is then washed away by the developer solution, leaving windows of the bare underlying material. Photoresist of approximately 2 ml is applied to

the clean surface of the substrate and spun-coat using a spinner at 2500 rpm (with a ramp of 500 rpm) for 30 seconds. High-speed centrifugal spinning of the substrate produces a thin uniform layer of photoresist on the substrate surface. This technique is known as “Spin Coating”.

(3) Soft baking: The substrate is rinsed in water and then soft-baked at 110 ˚C for 60 seconds. Soft-baking is a critical step in photolithography. Positive resists are incompletely exposed if considerable solvent remains in the coating. Softbaking removes solvents from the photoresist coating. The photoresist coatings become photosensitive, or imageable, only after softbaking. Over soft-baking will degrade the photosensitivity of resists by either reducing the developer solubility or actually destroying a portion of the sensitizer. Under soft-baking will prevent light from reaching the sensitizer.

(4) Mask Alignment: In this step, the mask is aligned with the substrate and the mask pattern is transferred onto the substrate surface. The alignment is accomplished using the alignment holes drilled on the substrate. The substrate is held on a vacuum chuck, and the whole assembly rises until the wafer and mask contact each other. The photoresist is exposed with UV light while the wafer is in contact position with the mask. Any debris trapped between the resist and the mask would cause defects in the pattern. So, care must be taken to avoid debris trapped between the mask and the substrate.

(5) Exposure: There are three primary exposure methods: contact, proximity, and projection. In this project, contact exposure method is used. In contact method, the resist-coated substrate is brought into physical contact with the glass photomask after alignment. The exposure dose for S1813 is 100-120 (mJ/cm^2) (Source: Microposit S1800 Series Photo resists, Shipley Company, Inc.,). If the UV lamp intensity is 10 mW/cm^2, then the exposure time must be in the range (100-120) (mJ/cm^2)/10 (mW/cm^2) = 10–12 seconds.

(6) Development: In positive photoresist, the portions of photoresist exposed to UV light become soluble in the developer solution. The substrate with the photoresist film is immersed in a container with CD-30 solution (available from Microchem Inc.,) and the features are developed.

(7) Hard baking: Hard-baking is the final step in the photolithographic process. This step is necessary in order to harden the photoresist and improve adhesion of the photoresist to the substrate surface. Hard-baking is done on a hot-plate at a temperature of 110°C for 60 seconds.

A.4.3 Etching

Conventional wet etching process of defining patterns by removal of the copper is used. In this project, CE-100 and CE-200 (available from Transene company) copper etchants with etching rates of 2 mil/min and 1 mil/min have been used. These etchants are isotropic in nature and therefore results in over-etching. This over-etching can be

compensated by oversizing strip patterns and undersizing slot openings with a correction factor. Over-etching depends on the required etching time and the etching time depends on the design (specifically on the total area of the copper to be removed). Masks with different values of over-etching correction factor, typically multiples of copper thickness, are prepared. After few etching tests, the mask that completely removes copper in the unwanted portions of the substrate and provides the required feature dimensions is identified. For duroid 6002 substrate with 9 µm, the over etching correction factor is about 25-30 microns and the etching time is in the range of 3:30 to 4:00 minutes with CE-200 copper etchant.

A.4.4 BCB coating Process

CYCLOTENE 4024-40 (available from Dow Chemical Company, Midland, MI), a photosesitive benzocyclobutene is used. Standard film thickness in the range of 3.5 – 7.5 microns can be obtained by spin-coating in the speed range of 1500-5000 rpm.

Application Procedure:

(1) Spinner speed 2500-3000 rpm, time=1:00 min. Surface cleaning using Acetone + methanol for 15 sec. Spin dry for 15 sec.

(2) Dispense 1 ml of adhesion promoter at the center of the spinning substrate and spin dry for 15-20 sec at 3000 rpm.

(2) Spinner speed 0 rpm, time=1:00 min. Dispense BCB.

(3) Spinner speed 500 rpm at 100 rpm ramp, time=5 sec. This step spreads out BCB resin.

(4) Spinner speed 800 rpm, time= 30 sec. This step provides the desired coating of 14-16 micron thickness.

A.4.4.1 UV Exposure

The substrate is baked (soft bake) in a hot plate @ 95°C, time=90 sec. The preexposure baking will drive out any residual solvent. The recommended UV light exposure dose is the range of 25 mJ/cm^2 for Cyclotene 4024-40. For an UV lamp intensity of 7 mW/cm^2, the required exposure time = (25 mJ/cm^2)*14μm / (7 mW/cm^2)/=50 seconds. The mask is aligned with the substrate and exposed to UV light for 50 seconds.

A.4.4.2 Development Procedure

(1) Spinner speed 50 rpm, time=5 sec. Dispense 2 ml of DS-2100 solvent on the substrate.

(2) Spinner speed 0000 rpm, time=25 sec. Stationary and dispense DS-2100 (say every 5 seconds)

(3) Spinner speed 1000 rpm, time=5 sec. Rinse the substrate using DS-2100.

(4) Spinner speed 2500 rpm, time= 30 sec. Spin dry the film.

A.4.4.3 Hard Bake

Hard bake the substrate in the hot plate @ 75°C for 60 seconds to thoroughly remove any residual solvent.

A.4.4.4 Curing

Two types of curing are possible for the BCB film. The procedures for different curings are shown in Figure A.2**.** Either type of curing is done in N_2 chamber. This step ensures chemical resistance of the film to subsequent processing operations.

step	soft cure	hard cure
1	15 min ramp to 150°C	15 min ramp to 150°C
2	15 min soak at 150°C	15 min soak at 150°C
3	ramp to 210°C	ramp to 250°C
4	40 min soak at 210°C	60 min soak at 250°C
5	cool to <150°C	cool to <150°C

Figure A.2. BCB Curing Procedures.

A.5 Switch membrane Layer

A.5.1 Top Electrode Patterning

The surface roughness value of the copper metallization on the I-flex film is about 0.1–0.15 µm (rms value). These values are acceptable for fabrication of flexible printed circuit based RF MEMS switches. Both sides of the I-flex film are processed to define identical copper electrode patterns.

Photolithography and Etching: To make the film stable to be able to perform photolithography on it, it is stuck on a Silicon substrate with a thermally conductive gel. This gel is an extremely important part of the fabrication process of the Kapton film since it also helps absorbs the heat generated during the DRIE etching process while keeping the film flat on the Silicon substrate without any bubbles. The top electrode patterns are defined by photolithography and etching processes. While performing the etching of the Nichrome layer, it is to be noted that the Nichrome etchant reacts with photoresist and produces an extremely difficult to remove compound. To reduce over-etching,

intermediate masks are used to remove the majority of the unwanted copper leaving behind rectangular or polygonal copper patches where small features can be defined in a later step. After all the features on the Kapton film have been defined, a 5000 Å thick Aluminium layer is deposited on top of the defined features side of the Kapton film and this Aluminium layer is patterned and etched as to expose only the Kapton that needs to be etched.

A.5.2 DRIE Etching

DRIE etching of the Kapton film is performed at Auburn University. The machine used for this process is an STS AOE (Advanced oxide etch) .The configuration of the gases used for this etch in our facility is 8 sccm CF_4 and 35 sccm Oxygen with 500 Watts of RF power. The ratio of the gases is the most important part and not the exact quantity of the gases. These processing parameters take about 70 minutes to etch a 2 mil thick Kapton layer. It is extremely important that the Kapton film is stuck to the Silicon substrate with the thermally conductive gel without any air bubbles. If air bubbles are present between the substrate and the film, it results in inconsistent etching of the Kapton film. Removal of the air bubbles is performed by manually applying pressure on the Kapton film stuck on the Silicon substrate and driving the air bubbles out on a hot plate at 110 ˚C.

A.6 Adhesive spacer film machining

The adhesive spacer film obtainable from Polyflon Company is machined using a vertical mill.

Appendix B A KOCH FRACTAL ANTENNA

B.1 Introduction

The use of fractal geometries in designing Antennas has been on the rise since the discovery of the improved characteristics fractal structures could provide. Characteristics such as reduction in size, multi-band operation, improvement in antenna efficiency and improved matching for low impedance antennas are always sought after in antenna design [30], [31]. The above mentioned characteristics have already been explored in microstrip antennas using fractal techniques but have not been extensively studied in slots antennas involving fractal geometries. Hence an effort has been made in this work to apply Koch fractal techniques to slot antennas.

B.2 Theory, Design and Results

A $\lambda/2$ slot antenna is designed on Duroid substrate (ε_r=2.94) with copper thickness of 9 µm. The length ℓ of the slot antenna is calculated using

$$l = \lambda / 2$$

The Koch iterations are performed on this antenna. Koch iteration lengths are dependant on the formulae for self similarity dimension given by [30]

$$D = \log n / \log(1/f)$$

where D is the fractal dimension, n is the number of copies scaled down by a fraction f. In this design, only one iteration of the Koch curve is being presented and hence n=4 and

f=3 which leads to D=1.26. In the following sections, Koch iterations are applied to the simple slot antenna design and results are discussed.

B.3 Simple Slot Antenna

Initially, a simple slot antenna design was designed with length ℓ = 11.6 mm and width w = 0.4 mm. The design has been simulated using Ansoft HFSS [27] and the 3D solid model is shown in Figure B.1. The performance of the simple slot antenna is shown in Figure B.2, Figure B.3, and summarized in

Table B.1.

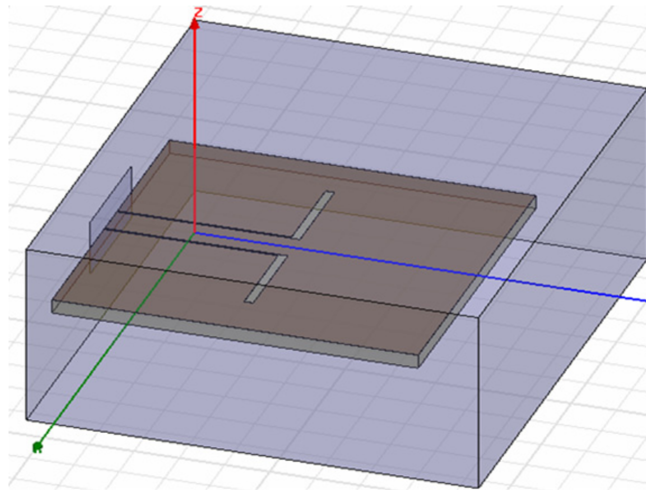

Figure B.1 A Simple Slot Antenna

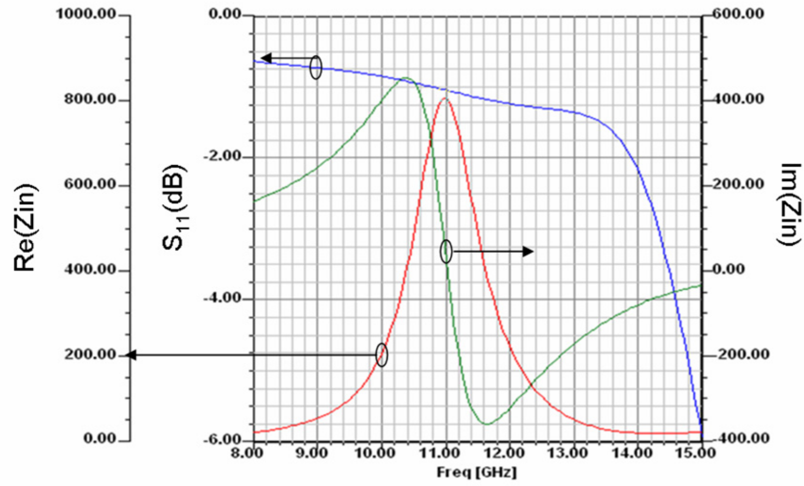

Figure B.2 Return Loss and Real and Imaginary parts of input impedance for the simple slot antenna.

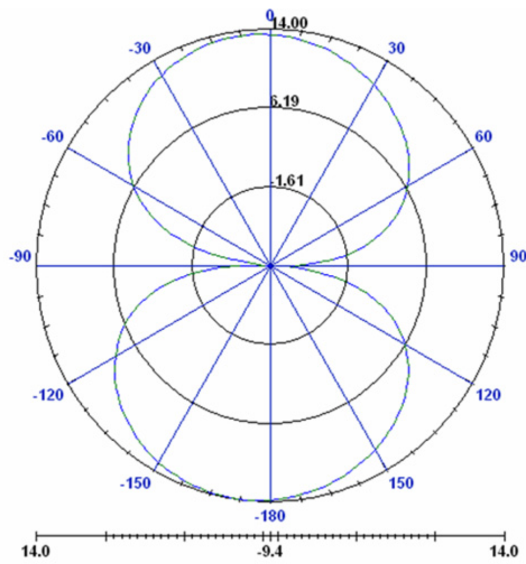

Figure B.3 Radiation Pattern for the simple slot Antenna (E Plane Co)

Table B.1 Resonant frequency, Return Loss and Input Impedance of an unmatched slot antenna

f_r(GHz)	S_{11}(dB)	Re(Zin)	Im(Zin)
11.03	-1	800	~0

B.4 Folded Slot Antenna

As can be seen from Table B.1, the input impedance of the slot antenna is extremely high making matching the antenna a very difficult proposition. To alleviate this problem, a folded slot antenna is designed with two slots, the input impedance of which is

$$Zin_f = Zin/n^2$$

where Zin_f is the input impedance of the folded slot antenna. 3D solid model and performance of the folded slot antenna with matching network are shown in Figure B.4, Figure B.5, Figure B.6 and Table B.2.

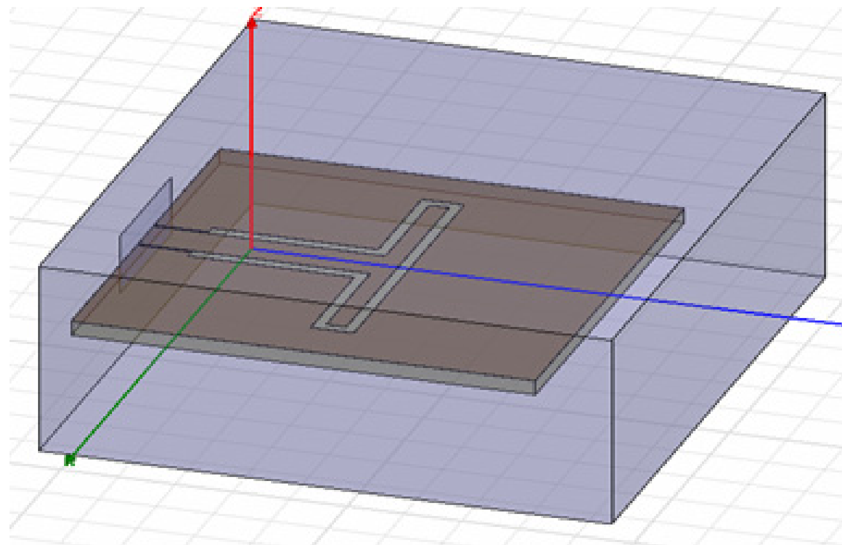

Figure B.4 Layout of a folded slot antenna

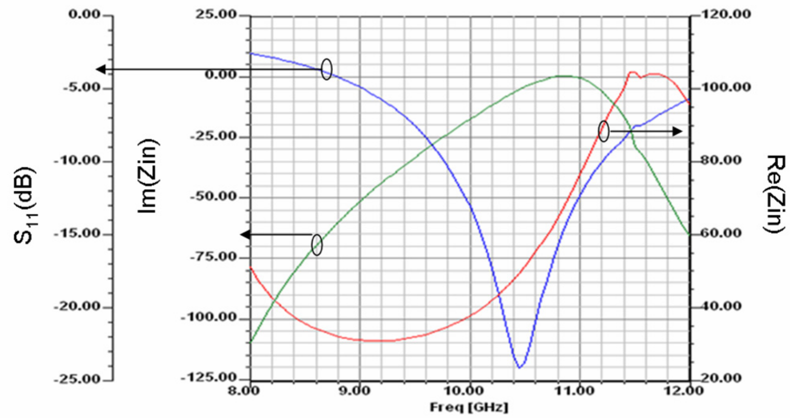

Figure B.5 Return Loss and Real and Imaginary parts of input impedance for a matched folded slot antenna.

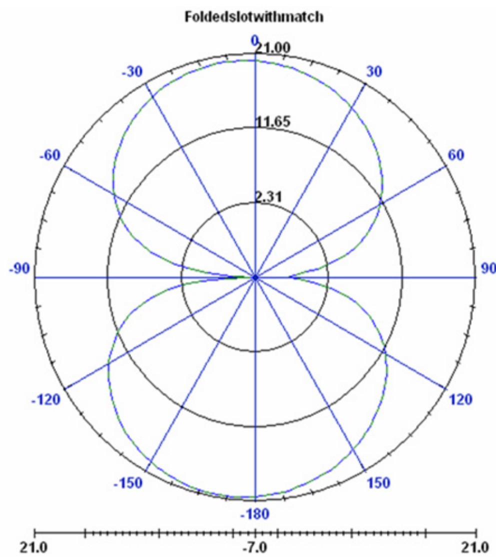

Figure B.6 Radiation Pattern for the folded slot Antenna (E plane Co).

Table B.2 Resonant frequency, Return Loss and Input Impedance of a matched folded slot antenna

f_r(GHz)	S_{11}(dB)	Re(Zin)	Im(Zin)
10.45	-24.05	49.69	-5.23

B.5 Folded Slot Antenna with Koch Iteration (type 1).

Koch Iterations are performed on the simple slot antenna design described in the previous section. In type 1 Koch Iteration, both slots in the antenna are subjected to the Koch Iteration, i.e., each slot is divided into four copies of a 3rd fraction of the original slot length. Since the CPW feed divides the bottom slot into two segments, these segments are treated as individual slots for Iteration purpose. The 3D solid model of the type 1 Koch iteration folded slot antenna shown in Figure B.7. The performance and radiation patterns for this antenna are shown in Figure B.8 and Figure B.9

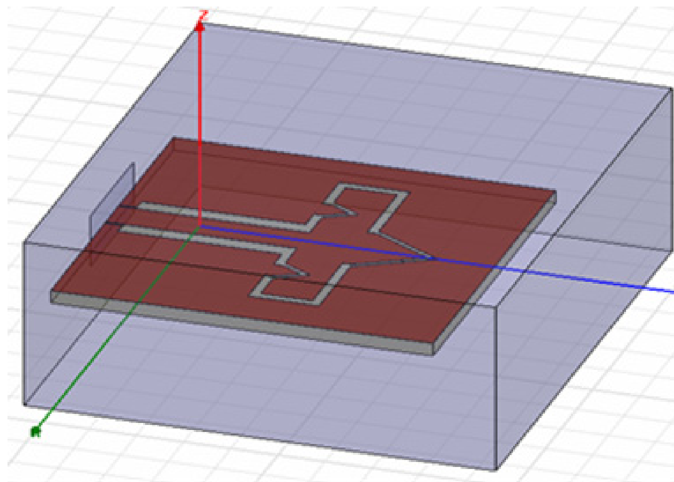

Figure B.7 Layout of a folded slot antenna with Koch Iteration (type 1).

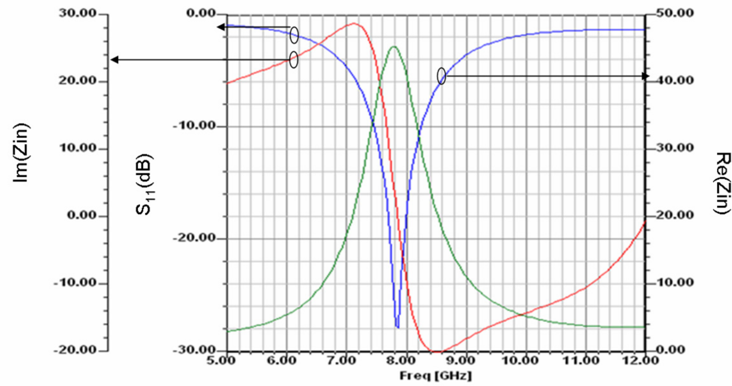

Figure B.8 Return Loss and Real and Imaginary parts of the input impedance for a matched folded slot antenna with 1st Koch Iteration (type 1).

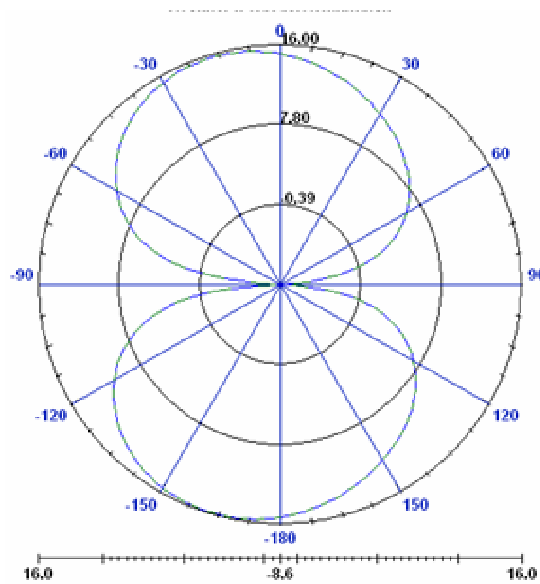

Figure B.9 Radiation Pattern for the folded slot Antenna with Koch iteration (type 1) (E plane Co)

Table B.3 Layout and performance of a matched type 1 Koch fractal slot antenna.

f_r(GHz)	S_{11}(dB)	Re(Zin)	Im(Zin)
7.82	-27	44.71	~0

It can be observed from Table B.2 and Table B.3 that because of the increase in length of the slot antenna caused by the Koch Iteration, the resonant frequency of the type 1 fractal antenna is much lower that that of the folded slot antenna. It is worth observing at this point that the E plane radiation pattern is tilted towards the feed side when the Koch iteration is applied.

B.6 Folded Slot Antenna with Koch Iteration (type 2)

In this formation, Koch iterations were performed on the bottom slot segments of the antenna. The 3D solid model and performance of this type of antenna is shown in Figure B.10, Figure B.11, Figure B.12 and Table B.4.

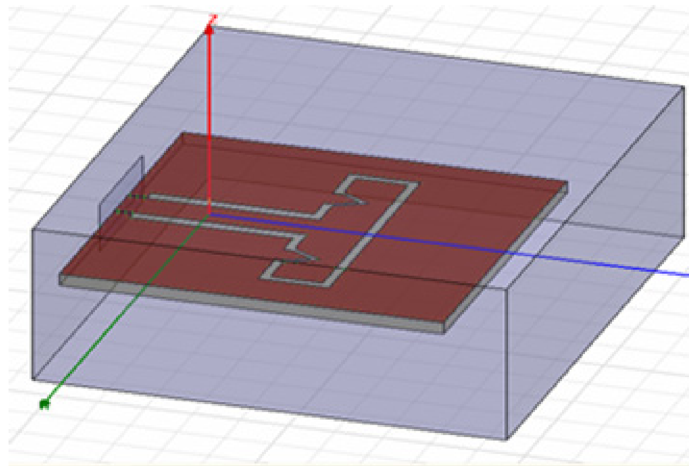

Figure B.10 Layout of a folded slot antenna with Koch Iteration (type 2).

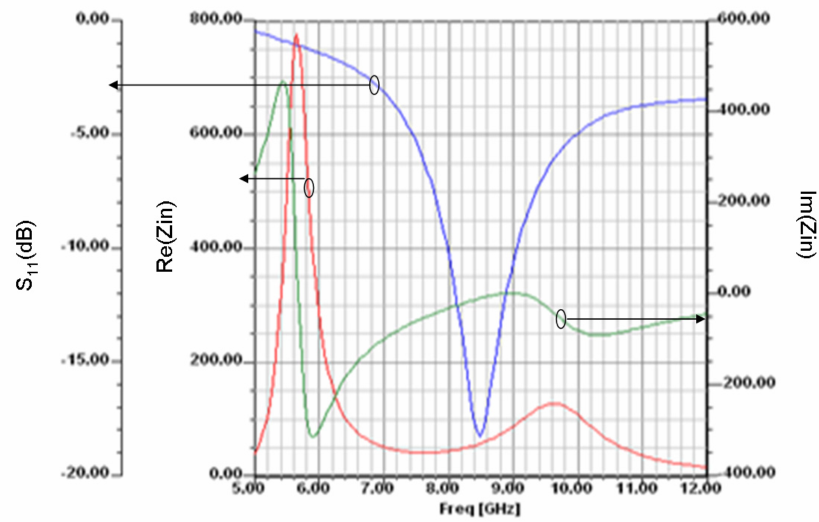

Figure B.11 Return Loss and Real and Imaginary parts of the input impedance for a matched folded slot antenna with 1st Koch Iteration (type 2)

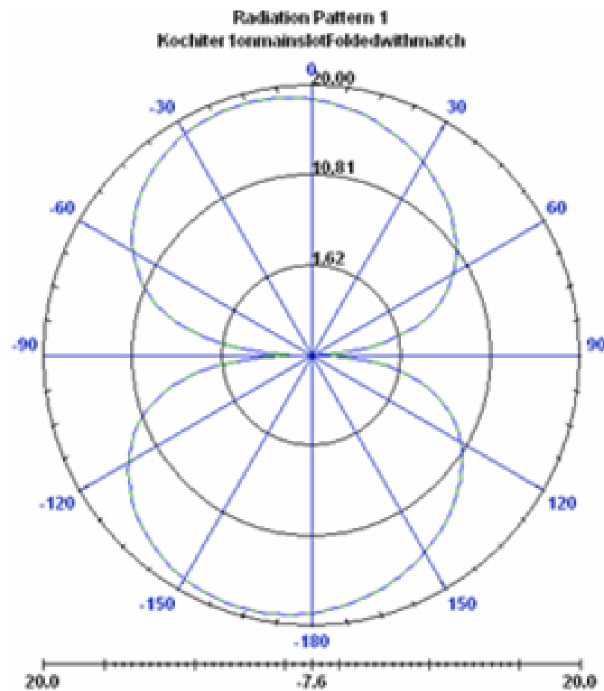

Figure B.12 Radiation Pattern for the folded slot Antenna with 1st Koch iteration (type 2) (E plane Co)

Table B.4 Layout and performance of a matched type 2 Koch fractal slot antenna.

f_r(GHz)	S_{11}(dB)	Re(Zin)	Im(Zin)
8.5	-18.2	57.89	-8.7

It can be seen from Table B.4 that removing the Koch Iteration from the upper slot of the antenna has increased the resonant frequency compared to type 1 antenna.

B.7 Folded Slot Antenna with Koch Iteration (type 3)

In the type 3 Fractal antenna, 1st Koch iteration is performed on both the top and the bottom slots as shown in Figure B.13.

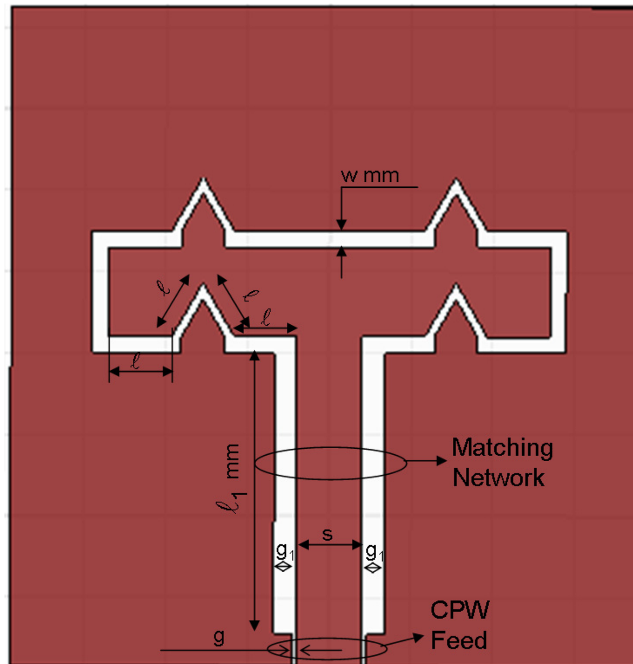

Figure B.13. Layout of a folded slot antenna with Koch Iteration (type 3).

The width of the slot is 0.4 mm and the Koch iteration length ℓ shown in the figure is 1.53 mm. The antenna is matched to a 50 Ω CPW feed line using an 82.5 Ω quarter wave transformer of length 6.9 mm. The dimensions g/s/g of the 50 Ω CPW feed line and 82.5 Ω quarter wave transformer sections are 0.1/1.6/0.1 mm and 0.55/1.6/0.55 mm, respectively.

The antenna was simulated in Ansoft HFSS® [27] and was fabricated using conventional photolithography techniques at the Auburn University's Microelectronics Center. Figure B.14 shows photograph of the fabricated antenna with MA46H203 varactor diode. Simulated and measured results for the return loss and radiation patterns of the antenna are shown Figure B.15 and Figure B.17, respectively. The return loss of the antenna was measured using an Agilent 8510C vector network analyzer. The calibration of the VNA was performed using 2.4 mm calibration standards. The antenna provides a return loss of around 34-35 dB at the operating frequency of 8.05 GHz. It can be noted that the simulated and measured return loss performances agree well at 8.05 GHz. The bandwidth of the antenna obtained from the measured return loss is about 0.3 GHz for a return loss better than 10 dB.

Figure B.14. Photograph of the fabricated Fractal Antenna with diode mounted for tuning purposes.

The radiation patterns of the antenna have been measured using the Desktop Antenna Measurement system available from Diamond Engineering. The antenna radiation patterns at the operating frequency of 8.05 GHz are shown in Figure B.17. It can be seen that the simulated and measured E-plane co-polarization, H-plane cross-polarization, and H-plane co-polarization patterns are in good agreement. The discrepancy between the simulated and measured E-plane cross-polarization patterns can be attributed to the interference of the feed line fields in the measured pattern.

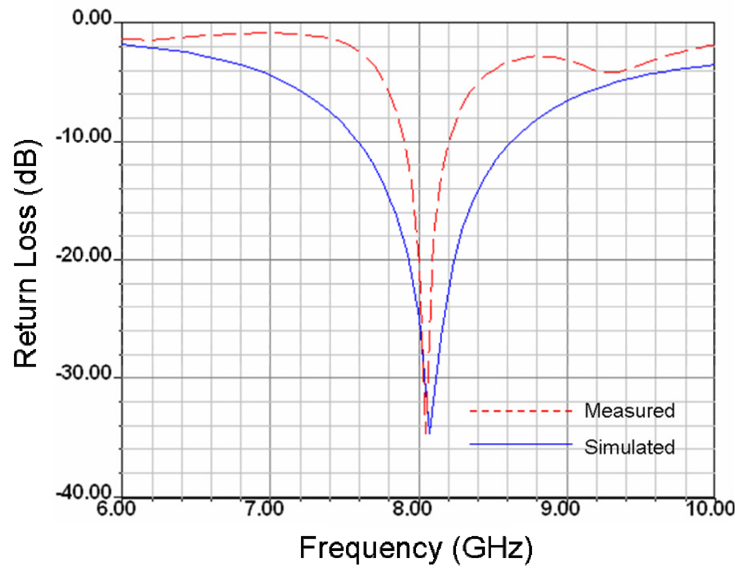

Figure B.15. Measured and Simulated return loss results for the type 3 Koch fractal antenna.

B.8 Tunable fractal folded Slot Antenna

The fractal antenna with type 3 Koch Iteration was tuned using a varactor diode. A varactor diode MA46H203 was mounted at the center of the top slot of the antenna as shown in Figure B.14. Typical capacitance range for the MA46H203 is 11 pF at 0.5 Volts and 1 pF at 20 Volts in reverse bias. At 0 V, the slot is capacitively loaded by the varactor and hence the operating frequency of the antenna would decrease when compared to the unloaded case. As the reverse bias voltage to the varactor diode is increased, the capacitive loading decreases and thereby increases the resonant frequency of the antenna. Figure B.16 shows the return loss results obtained for various bias voltages (0 to 18 V) applied to the varactor. The measurements were performed using an HP8510C network analyzer. It can be noted that as the reverse bias voltage to the varactor diode is increased the operating frequency of the antenna increases. The operating frequency of the antenna

increases from 7.98 GHz at 0 V to 8.05 GHz at 18 V providing a tuning range of 70 MHz. The return loss of the antenna is 47 dB and 20 dB at 7.98 GHz and 8.05 GHz, respectively. The return loss is better than 20 dB in the tunable frequency range of 7.98 GHz to 8.05 GHz. It should be pointed out that the operating frequency (8.05 GHz) of the antenna at 18 V corresponds to the operating frequency of the unloaded fractal antenna shown in Figure B.15.

Measured E-plane and H-plane radiation patterns of the antenna for various reverse bias voltages are shown in Figure B.18. The radiation patterns for each bias voltage were measured at the corresponding operating frequency of the antenna. The profiles of the measured radiation patterns for various bias voltages are in good agreement. It can be noted that as the bias voltage is increased the return loss decreases and hence the magnitudes of the radiation patterns decreases.

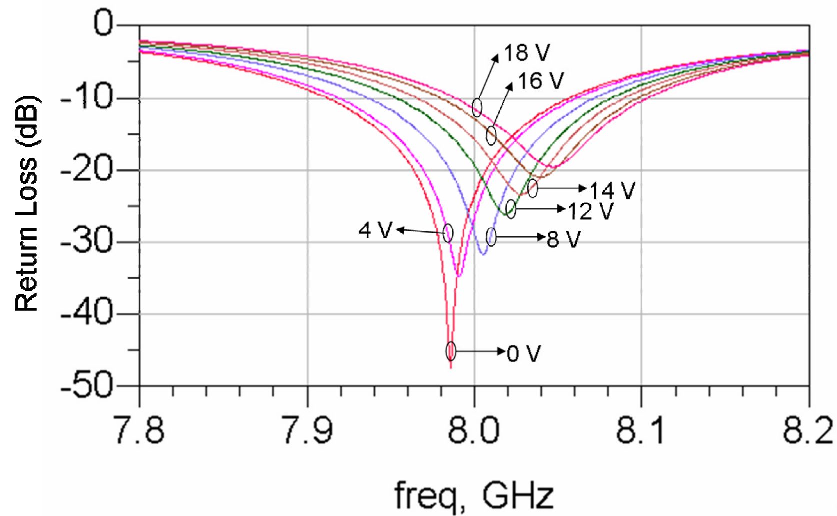

Figure B.16. Return losses of the tunable fractal antenna for various applied bias voltages.

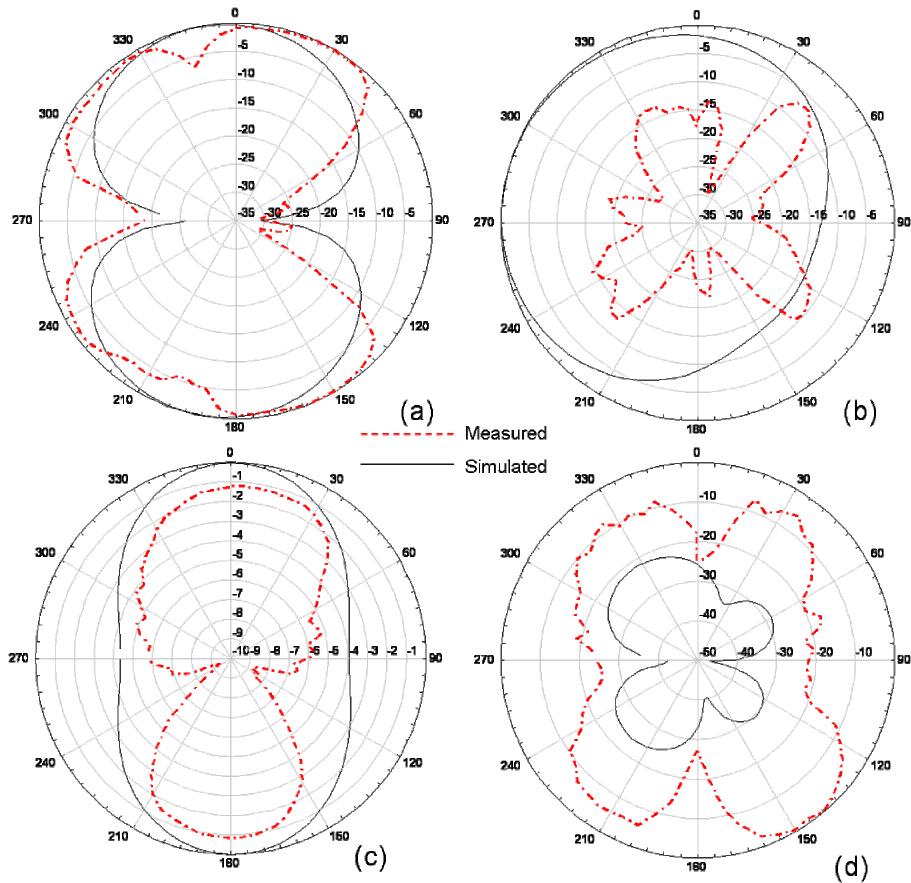

Figure B.17. Measured and Simulated antenna radiation patterns for the first iteration Koch fractal antenna at 8.05 GHz (a) E-plane co-polarization (E_θ) pattern, (b) E-plane cross-polarization (E_ϕ) pattern, (c) H-plane co-polarization (H_θ) pattern, and (d) H-plane cross-polarization (H_ϕ).

B.9 Discussion and Conclusion

It has been observed in this study of Koch fractals combined with slot structures that with the increase in the number of iterations, the input impedance of the slot antenna structure also increases which is because of the irregularity of the structure generated by Koch Iterations. Multi-band characteristics can be observed if the number of iterations on the slots are increased which was beyond the scope of this work. Another observation worth pointing out is that if the lengths of the edges of the slots are decreased after the iterations

are performed, the length of the antenna can be reduced to match with the normal slot antenna, reducing the area occupied by the overall structure. Radiation efficiencies for these structures were found to be very similar to those of a normal slot structures. Future work will focus on increasing the number of Koch iterations performed on the structures to observe multi-band performance and the change in radiation efficiency.

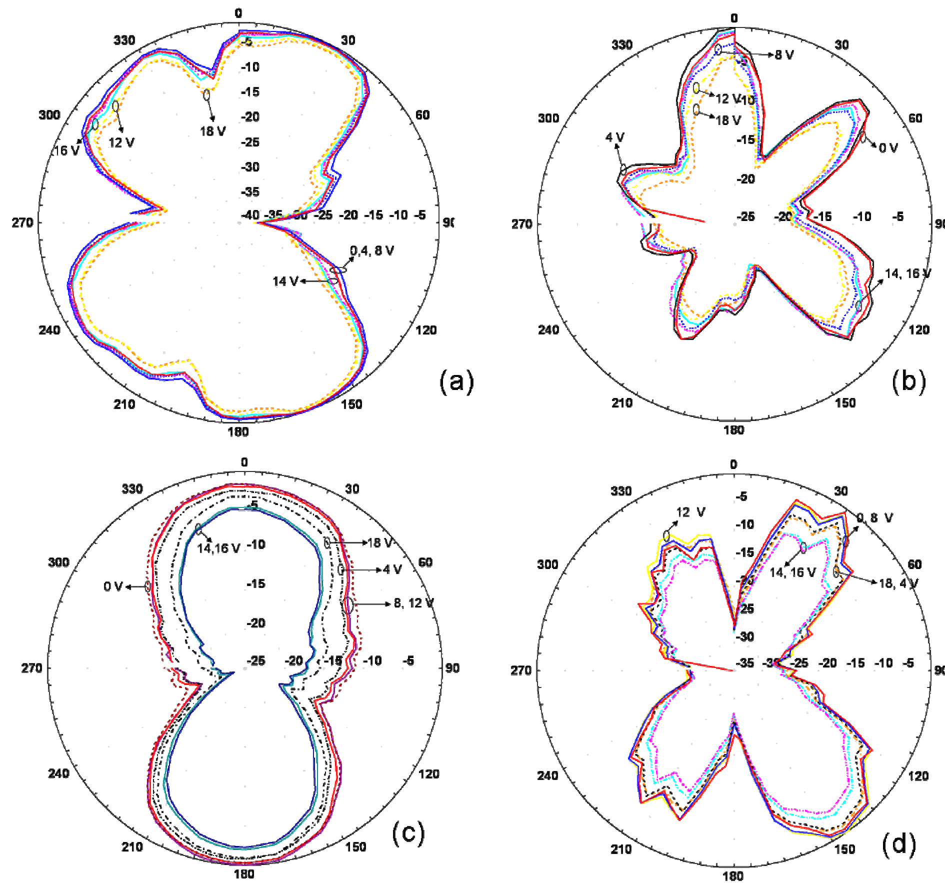

Figure B.18. Measured antenna radiation patterns for the tunable CPW Koch fractal Antenna at different frequencies corresponding to the bias voltages. (a) E plane co-polarization, (b) E plane cross-polarization, (c) H plane co-polarization and (d) H plane cross-polarization.